Coupling systems biology with multiscale mechanics, for computer simulations of bone remodeling

Stefan Scheiner [a,b,*], Peter Pivonka [a], Christian Hellmich [b]

[a] *Faculty of Engineering, Computing and Mathematics, The University of Western Australia, 35 Stirling Highway, Crawley, WA 6009, Australia*
[b] *Institute for Mechanics of Materials and Structures, Vienna University of Technology, Karlsplatz 13/202, A-1040 Vienna, Austria*

ABSTRACT

Bone remodeling is a process involving removal of mature bone tissue and subsequent formation of new bone tissue. This process is driven by complex actions of biological cells and biochemical factors, and it is sensitive to the loads applied onto the skeleton. Herein, we develop a mathematical framework describing this process at the (macroscopic) level of cortical bone, by combining, for the first time, bone cell population kinetics with multiscale bone mechanics. Key variables are concentrations of biological cells (osteoclasts, osteoblasts and their progenitors) and biochemical factors (RANK, RANKL, OPG, PTH, and TGF-β), as well as mechanical strains, both at the ("macroscopic") level of cortical bone and at the ("microscopic") level of the extravascular bone matrix. Multiscale bone mechanics delivers, as a function of the vascular porosity, the relation between the macroscopic strains resulting from the loads, and the microscopic strains, which are known to modulate, either directly, or via poromechanical couplings such as hydrostatic pressure or fluid flow, the expression or proliferation behavior of the biological cells residing in, or attached to the extravascular bone matrix. Hence, these microscopic strains enter the biochemical kinetics laws governing cell expression, proliferation, differentiation, and apoptosis. Without any additional phenomenologically motivated paradigm, this novel approach is able to explain the experimentally observed evolutions of bone mass in postmenopausal osteoporosis and under microgravity conditions: namely, a decrease of bone loss over time.

© 2012 The Authors. Published by Elsevier B.V. Open access under CC BY-NC-ND license.

1. Introduction

Bone remodeling is a process involving removal of mature bone tissue and subsequent formation of new bone tissue. This process allows for removal of microcracks endangering the mechanical integrity of the system, as well as for provision of mineral homeostasis in the skeleton [1–4]. Bone remodeling is undertaken by teams of biological cells. Once activated, osteoclasts remove bone tissue, leaving a cavity, which is thereafter filled by another cell type, osteoblasts. More precisely, the latter lay down osteoid, a material mainly composed of type I collagen that becomes mineralized over time. The tuned cooperation of osteoclasts and osteoblasts often leaves spatial patterns in histological sections of cortical bone, called, after Frost [5], bone multicellular units (BMUs). The aforementioned tuning, however, is largely influenced by a third cell type, osteocytes [6–10], which originate from buried osteoblasts, and reside in lacunar pores inside the bone tissue. They maintain, via long cell processes, connections with the cells at the bone matrix surfaces, as well as with other osteocytes, thus making up a large network. Osteocytes respond to both biochemical factors (e.g. hormones and local cytokines) and mechanical stimuli (induced by deformation of the bone matrix), both of which are subsequently "translated" into biochemical signals regulating the behavior of cells within BMUs.

An imbalance between bone resorption and bone formation (triggered by perturbance of biochemical and/or mechanical regulation mechanisms) can lead to significant structural changes within bone and so (adversely) affect its load-carrying capacity. However, despite intensive research activity for decades, current understanding of BMU regulation and associated changes in mechanical properties of bone is still fragmented due to complex (feedback-type) interrelationships between bone cells and structural features of bone. Given this inseparable interplay, identifying mechanisms which coordinate the cell behaviour in BMUs and predicting changes in mechanical properties of bone requires a synergistic approach combining mathematical modeling and experimental testing [11,12].

Most of previous mathematical models have focused on describing the mechanical properties of bone using numerical approaches, such as the Finite Element method or molecular dynam-

* Corresponding author at: Institute for Mechanics of Materials and Structures, Vienna University of Technology, Karlsplatz 13/202, A-1040 Vienna, Austria. Tel.: +43 1 58801 20265.
E-mail address: stefan.scheiner@tuwien.ac.at (S. Scheiner).

ics simulations [13–18]. As a computationally very efficient complement to these techniques, Hellmich and co-workers have proposed analytical and semi-analytical models for estimating bone stiffness, bone strength, and poroelastic properties of bone, based on the concept of multiscale continuum micromechanics [19–22]. These models take the hierarchical organization of bone into account, and are based on the volume fractions of the different bone constituents, their mechanical properties and their mechanical interactions.

In standard micromechanical applications, the constituent volume fractions are known as input values. However, during bone metabolism, the volume fractions change, and the question arises how to determine these changes. In order to answer this question, which is at the very focus of this paper, we note that the aforementioned volume fractions are either directly linked to chemical processes (such as biomineralization, when hydroxyapatite crystals precipitate inside a network of collagen molecules [23]) or to cellular activity (such as bone remodeling, when e.g. the volume fraction of bone tissue inside a piece of cortical bone changes); and that recently, the challenge of mathematically describing the biology and biochemistry of bone remodeling has been quite successfully met [24–26], in the framework of bone cell population models (BCPMs). Such models allow for estimation of temporal changes in bone cell numbers during bone remodeling, interpretable in terms of the corresponding evolution of the bone volume over time. While such BCPMs were previously used to give valuable information on the effects of bone disease and/or therapeutic treatment scenarios, one key novelty of the present paper is to use the output of BCPMs as input for bone micromechanics formulations.

However, also the (local) mechanical environment of osteocytes governs bone remodeling. Properties quantifying this mechanical environment can be derived from multiscale micromechanical models. This relates to the second key novelty of this paper, namely the extension of state-of-the-art BCPMs to micromechanically quantified strain stimuli.

With these conceptual novelties at hand, we address a fundamental question in bone biology:

Can bone remodeling, often associated to some "mechanostat-paradigm" with corresponding tuning parameters [27–29], be explained solely by combined effects of multiscale mechanics and bone cell population kinetics, which are exclusively based on physical properties such as chemical concentrations, volume fractions, geometrical shapes, and mechanical properties?

An attempt of a quite comprehensive answer to this question is made hereafter, within the following structure of the remaining paper: first, we introduce the mathematical systems biology of bone, starting from the work of Pivonka et al. [25,26], and extending it to mechanoregulatory feedback control (Section 2). Then, we introduce a continuum micromechanics representation adopted from Hellmich et al. [30], in order to scale elasticity and strains from the level of the extravascular bone matrix to that of cortical bone[1] and vice versa (Section 3). The micromechanics formulation is fed with composition quantities derived from the systems biology approach, which, in turn, is provided with mechanical stimuli gained from the micromechanics model. We then apply the coupled approach to biochemical and mechanical conditions typical for postmenopausal osteoporosis (Section 4) and microgravity exposure (Section 5), and discuss key sensitivity features (Section 6). After emphasizing the potentials and limitations of the presented approach (Section 7), we conclude the paper in (Section 8).

2. Mathematical systems biology of bone

Adopting the choice made by Pivonka et al. [25,26], we explicitly consider the following types of bone cells (see Fig. 1): uncommitted osteoblast progenitors cells, also referred to as bone marrow stromal cells or mesenchymal stem cells (abbreviated to OB_u); osteoblast precursor cells, also referred to as preosteoblasts (OB_p); active osteoblasts (OB_a); osteoclast precursor cells, also referred to as preosteoclasts (OC_p); and active osteoclasts (OC_a). As an original contribution of the present work, we extend the approach of [25,26] to mechanoregulation. Hence, the following equations for the evolutions of the aforementioned bone cell populations (expressed in terms of molar concentrations C_i) contain not only biochemical, but also mechanobiological activator and repressor functions.

2.1. Evolution of osteoblasts

The evolution of the osteoblast precursor cells is quantified by the following kinetics law:

$$\frac{dC_{OB_p}}{dt} = \mathcal{D}_{OB_u} C_{OB_u} \pi_{act,OB_u}^{TGF-\beta} + \mathcal{P}_{OB_p} C_{OB_p} \Pi_{act,OB_p}^{mech} - \mathcal{D}_{OB_p} C_{OB_p} \pi_{rep,OB_p}^{TGF-\beta}. \quad (1)$$

In this mathematical formulation, we explicitly consider that the population of osteoblast precursor cells in a piece of cortical bone increases due to differentiation (with maximum differentiation rate $\mathcal{D}_{OB_u}$) of uncommitted osteoblast progenitor cells – this differentiation is promoted by transforming growth factor β, TGF-β [3,31], quantified by activator function $\pi_{act,OB_u}^{TGF-\beta}$, see Eq. (A.1) in Appendix A. Furthermore, the population of osteoblast precursor cells decreases due to differentiation (with maximum differentiation rate $\mathcal{D}_{OB_p}$) of osteoblast precursor cells into active osteoblasts – this differentiation is inhibited by TGF-β [3,31], as quantified by repressor function $\pi_{rep,OB_p}^{TGF-\beta}$, see Eq. (A.2) in Appendix A.

As a conceptual novelty, we introduced, in Eq. (1), an additional term, which is related to proliferation of osteoblast precursor cells (with maximum proliferation rate $\mathcal{P}_{OB_p}$), promoted by mechanical strains in the extravascular bone matrix, as quantified through the activator function Π_{act,OB_p}^{mech}. Current literature suggests at least two mechanisms by which osteoblast precursor cells may respond to mechanical stimuli: (i) directly via cell stretching due to matrix deformation and/or fluid flow [32,33], and (ii) indirectly via biochemical signals (such as sclerostin) derived from osteocytes [6,34–36]. Both of these mechanisms are thought to regulate preosteoblast proliferation. For the purpose of our study we do not further specify which of these mechanisms prevails, but employ a phenomenological activator function Π_{act,OB_p}^{mech} to regulate proliferation of preosteoblasts. As a straightforward scalar measure for the strains in the extravascular matrix, we choose the strain energy density (SED) in the extravascular bone matrix, Ψ_{bm} – this choice is inspired by classical contributions to the field of mechanobiology [37–39]. The SED Ψ_{bm} at the bone matrix level depends on the loading of the considered piece of cortical bone, as well as on this piece's microstructure and its vascular porosity – these relations can be quantified by means of the micromechanics representation given in Section 3. Also, we restrict ourselves to explicit consideration of strain amplitudes only, thereby taking a (constant) physiologically relevant frequency [6,40] as granted.

According to Eq. (1), the maximum proliferation rate $\mathcal{P}_{OB_p}$ is related to the maximum value of Π_{act,OB_p}^{mech}, $max(\Pi_{act,OB_p}^{mech}) = 1$, and this maximum rate is attained upon sufficient mechanical activation of the osteoblasts. Low straining reduces the proliferation rate by some 25% to 50% according to the experiments of Jones et al. [41] and Kaspar et al. [42]; and this is considered by setting the minimum value of Π_{act,OB_p}^{mech}, related to a threshold SED $\hat{\Psi}_{bm}$, only

---

[1] In this paper, we restrict ourselves to cortical bone, due to its major importance in providing sufficient load-carrying capacity. However, extension of the coupled approach proposed here to trabecular bone is straightforward; it merely requires recalibration of underlying parameters.
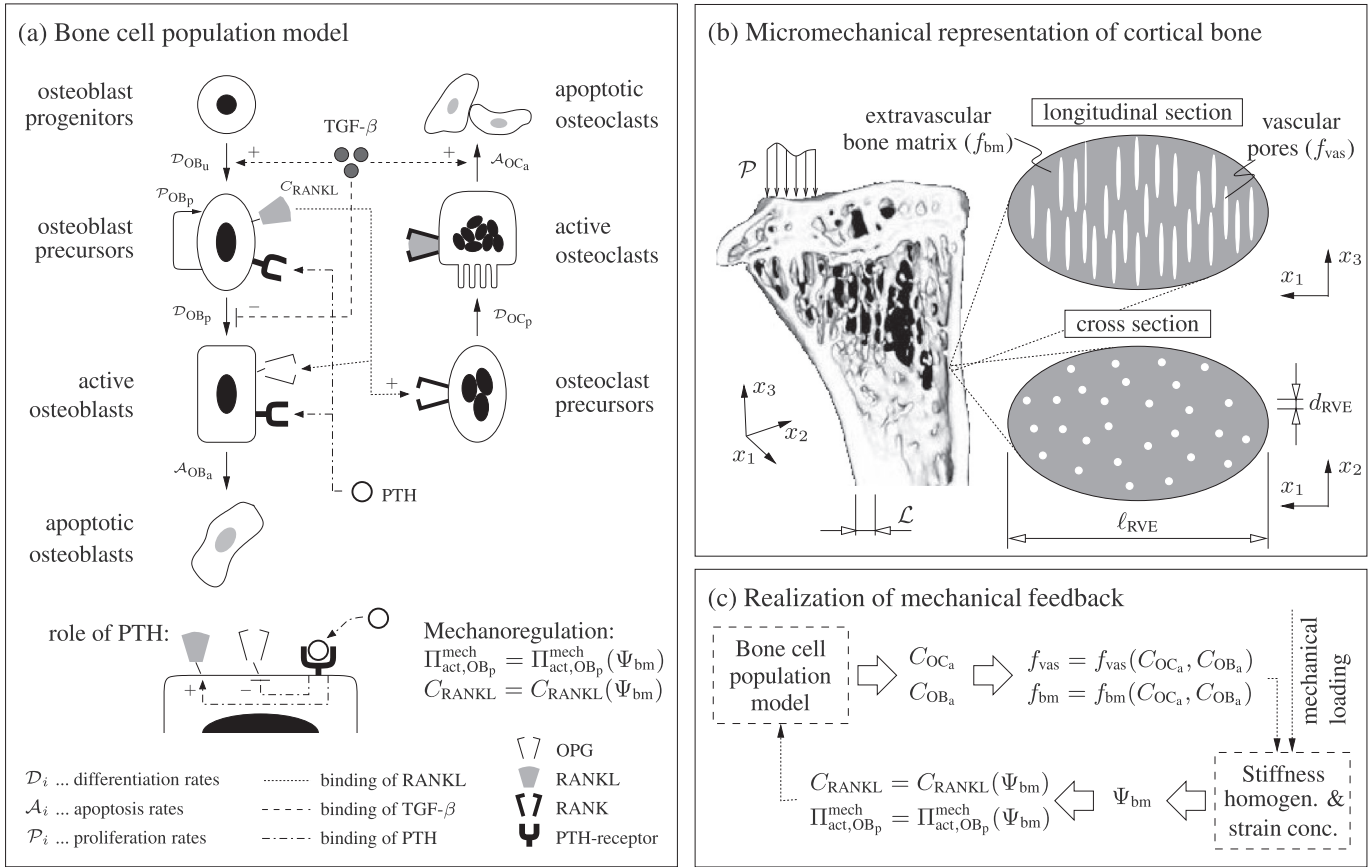
Fig. 1. (a) Sketch of the bone cell population model and involved differentiation, proliferation and apoptosis pathways, as well as the biochemical regulators (+/ −…biochemical activation/repression), see Section 2 and Appendix A for details; (b) micromechanical representation of cortical bone (picture reproduced from www.bme.ccny.cuny.edu) with constituents "vascular pores" and "extravascular bone matrix" and corresponding volume fractions f_{vas} and f_{bm}, requiring fulfillment of the separation of scales-requirement: $d_{RVE} \ll \ell_{RVE} \ll \{\mathcal{L}, \mathcal{P}\}$, with $d_{RVE} = 50 \dots 80 \times 10^{-6}$ m and $\ell_{RVE} = 1 \dots 3 \times 10^{-3}$ m, see Section 3.1 for details; (c) mechanoregulatory feedback: the concentrations of active osteoblasts and active osteoclasts, C_{OB_a} and C_{OC_a}, govern the change of f_{vas} and f_{bm} (see Section 3.2), which, under the prevailing mechanical loading, leads to cell-affecting changes in strain energy density Ψ_{bm}, see Sections 2 and 3 for details, in particular Eqs. (2), (5), (14), and (15).

above which increased proliferation of preosteoblasts is activated, to $\min(\Pi_{act,OB_p}^{mech}) = \check{\Pi}_{act,OB_p}^{mech} = 0.5$. Between minimum and maximum proliferation rate, we here introduce a linear relation, somehow reminiscent of the work by Sanz-Herrera et al. [43],

$$\Pi_{act,OB_p}^{mech} = \check{\Pi}_{act,OB_p}^{mech}\left[1 + \lambda\left(\frac{\Psi_{bm}}{\check{\Psi}_{bm}} - 1\right)\right], \tag{2}$$

which is valid for $\check{\Psi}_{bm} \leqslant \Psi_{bm} \leqslant \hat{\Psi}_{bm}$, with $\hat{\Psi}_{bm} = \{\check{\Psi}_{bm}[1 - \check{\Pi}_{act,OB_p}^{mech}(1 - \lambda)]/(\lambda\check{\Pi}_{act,OB_p}^{mech})\}$, λ being an "anabolic strength parameter". Furthermore, $\Pi_{act,OB_p}^{mech} = \check{\Pi}_{act,OB_p}^{mech}$ if $\Psi_{bm} \leqslant \check{\Psi}_{bm}$, and $\Pi_{act,OB_p}^{mech} = 1$ if $\Psi_{bm} \geqslant \hat{\Psi}_{bm}$, see Fig. 2(a). Parameter λ determines the slope of function $\Pi_{act,OB_p}^{mech} = \Pi_{act,OB_p}^{mech}(\Psi_{bm})$, $\lambda = (d\Pi_{act,OB_p}^{mech}/d\Psi_{bm})/(\check{\Pi}_{act,OB_p}^{mech}/\check{\Psi}_{bm})$, thus, λ defines for which increase of Ψ_{bm}, associated to a corresponding increase of the mechanical load, $\Pi_{act,OB_p}^{mech} = 1$ is reached, e.g. $\lambda = 1$ implies that increasing the SED by 100% (with respect to the threshold value $\check{\Psi}_{bm}$), i.e. $\hat{\Psi}_{bm}/\check{\Psi}_{bm} = 2$, is required for maximizing the proliferation activator function, from $\check{\Pi}_{act,OB_p}^{mech}$ to $\max(\Pi_{act,OB_p}^{mech}) = 1$, whereas $\lambda = 4$ implies that $\max(\Pi_{act,OB_p}^{mech})$ is already reached for an increase of Ψ_{bm} by 25%, i.e. $\hat{\Psi}_{bm}/\check{\Psi}_{bm} = 1.25$. Computational studies presented later in this paper, see Sections 4 and 6, show that setting $\lambda = 1.25$ allows us to simulate the physiological behavior of bone during osteoporosis and disuse scenarios.

The evolution of active osteoblasts is quantified through the following kinetics law:

$$\frac{dC_{OB_a}}{dt} = \mathcal{D}_{OB_p}C_{OB_p}\pi_{rep,OB_p}^{TGF-\beta} - \mathcal{A}_{OB_a}C_{OB_a}, \tag{3}$$

considering that the population of active osteoblasts is increased by differentiation (with maximum differentiation rate $\mathcal{D}_{OB_p}$) of osteoblast precursor cells (which is inhibited by TGF-β, as described before), and that the population is reduced by active osteoblast apoptosis (with apoptosis rate $\mathcal{A}_{OB_a}$).

2.2. Evolution of osteoclasts

The evolution of active osteoclasts is quantified through the following kinetics law:

$$\frac{dC_{OC_a}}{dt} = \mathcal{D}_{OC_p}C_{OC_p}\pi_{act,OC_p}^{RANKL} - \mathcal{A}_{OC_a}C_{OC_a}\pi_{act,OC_a}^{TGF-\beta}, \tag{4}$$

i.e. we explicitly consider that active osteoclast apoptosis (with maximum apoptosis rate $\mathcal{A}_{OC_a}$) is activated by TGF-β [44], see Eq. (A.3) in Appendix A. On the other hand, the population of active osteoclasts increases due to differentiation of osteoclast precursor cells (with maximum differentiation rate $\mathcal{D}_{OC_p}$), activated by RANKL (i.e., the ligand of RANK – the receptor activator of nuclear factor kappa β). The corresponding activator functions, π_{act,OC_p}^{RANKL} and $\pi_{act,OC_a}^{TGF-\beta}$, respectively, are defined in Appendix A, in Eqs. (A.5) and (A.3), respectively.

As a novel feature with respect to the formulation of Pivonka et al. [25,26], we here consider production of RANKL through the
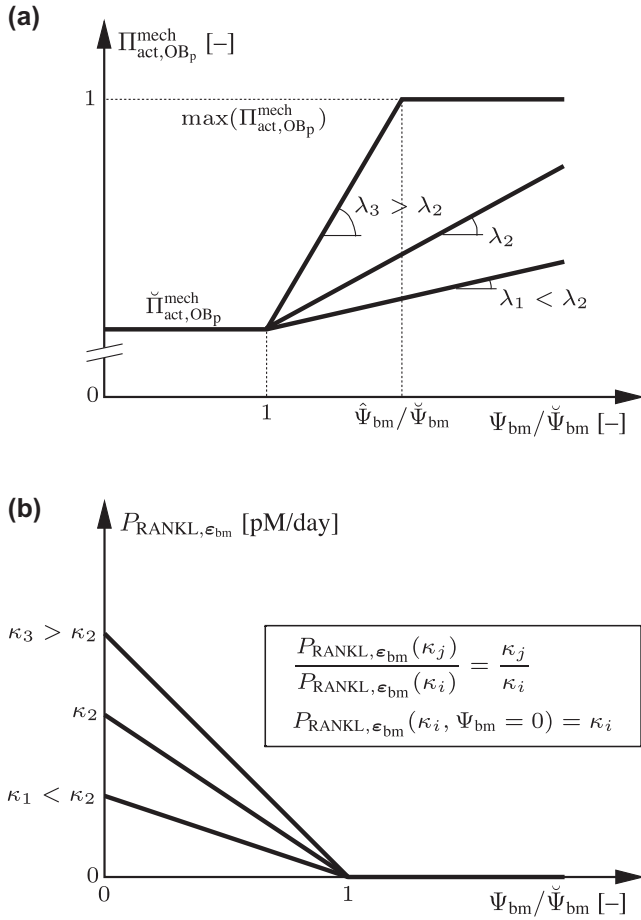
(a)

(b)

Fig. 2. Model implementation of mechanoregulation: (a) mechanical proliferation activator function $\Pi_{\mathrm{act,OB_p}}^{\mathrm{mech}}$, defined by Eq. (2), plotted for three different anabolic strength parameters $\lambda, \lambda_1 < \lambda_2 < \lambda_3$; and (b) mechanically regulated dosage of RANKL, $P_{\mathrm{RANKL},\varepsilon_{\mathrm{bm}}}$, defined by Eq. (5), plotted for three different inhibition parameters $\kappa, \kappa_1 < \kappa_2 < \kappa_3$.

osteocytes residing in the lacunar pores which are uniformly distributed throughout the extravascular bone matrix. The biochemical activity of the latter is again linked to mechanical straining of the extravascular bone matrix, in at least three different ways: (i) the osteocytes are directly strained, (ii) they are subjected to hydrostatic pressure, and (iii) the fluid around them starts to flow. All three effects have been shown to affect the biochemical behavior of the osteocytes: Cyclic hydraulic pressure has been shown to decrease the RANKL/OPG ratio expressed by osteocytes [45]. Direct straining in the physiological range of thousand microstrains,[2] as well as exposure to pulsating fluid flow, promote nitric oxide (NO) production by the osteocytes [49,50], and NO is known to decrease the RANKL/OPG ratio expressed on bone marrow stromal cells [51,52]. This overall inhibition of RANKL through bone matrix strains is considered here by means of the RANKL dosage term P_{RANKL}, entering Eq. (A.7) and thus regulating $\pi_{\mathrm{act,OC_p}}^{\mathrm{RANKL}}$ through Eqs. (A.5) and (A.6). In our model, P_{RANKL} is chosen to be of the form

$$P_{\mathrm{RANKL}} = P_{\mathrm{RANKL},\varepsilon_{\mathrm{bm}}} = \kappa\left(1 - \frac{\Psi_{\mathrm{bm}}}{\breve{\Psi}_{\mathrm{bm}}}\right), \qquad (5)$$

with a (non-zero) inhibition parameter κ if $\Psi_{\mathrm{bm}} < \breve{\Psi}_{\mathrm{bm}}$, and total inhibition related to $\kappa = 0$ if $\Psi_{\mathrm{bm}} \geqslant \breve{\Psi}_{\mathrm{bm}}$, see Fig. 2(b). Eq.

---

[2] Note that physiological strains defined at the level of extravascular bone matrix are increased by a factor of around three when reaching the local osteocyte level [46,47], and also strain amplification mechanisms for fluid drag-induced movements have been proposed [48].

(5) expresses mathematically that any straining restricts "external" RANKL production by osteocytes and bone marrow stromal cells [53], and the latter is totally stopped once the aforementioned critical (threshold) value $\breve{\Psi}_{\mathrm{bm}}$ of the SED is reached. Experiment-based determination of the exact value of κ is difficult (if not impossible), due to the involved uncertainties and the discrepancies between realizable experimental models and the physiology of human bone. However, experimental studies [54] allow us to infer that RANKL doses, for physiologically relevant disuse scenarios, relating to κ varying between 10^3 and 10^5 pM/day, are able to facilitate the activity of osteoclasts. Numerical studies on mechanoregulation during a disuse scenario (see Section 5) showed that setting $\kappa = 10^5$ pM/day gives rise to a model-predicted porosity evolution which agrees with physiological observations.

We note in passing that Eqs. (2) and (5) may be replaced by appropriate Hill-type (logistic) functions, if deemed favorable. As mentioned before, Ψ_{bm} is accessible from a micromechanical representation of cortical bone, which is presented next.

3. Microstructure-based scaling of elasticity and strains in cortical bone

As basis for the following developments, we adopt the micromechanical representation of bone proposed by Hellmich et al. [30], see Section 3.1 for details. As an original contribution of the present work, we couple the volume fractions entering the aforementioned micromechanical model, to the osteoblastic and osteoclastic cell populations (see Section 3.2), and we use the micromechanical model not only for homogenization from the sub-millimeter to the millimeter scale, but also for concentration from the millimeter scale down to the scale of extravascular bone matrix, as described in Sections 3.3 and 3.4.

3.1. Representative volume element and micromechanical representation of cortical bone

In order to establish the relation between the "macroscopic" strains acting on a piece of cortical bone and the "microscopic" strains in the extravascular matrix (the latter strains stimulating, through different mechanisms including fluid flow, the osteocytes embedded in this matrix), we employ the concept of continuum micromechanics [55–58], where a material is understood as a macro-homogeneous, but micro-heterogeneous body filling a representative volume element (RVE) with characteristic length $\ell_{\mathrm{RVE}}, \ell_{\mathrm{RVE}} \gg d_{\mathrm{RVE}}, d_{\mathrm{RVE}}$ representing the characteristic length of inhomogeneities within the RVE, see Fig. 1(b), and $\ell_{\mathrm{RVE}} \ll \{\mathcal{L}, \mathcal{P}\}, \mathcal{L}$ representing the characteristic length of the geometry and $\mathcal{P}$ representing the characteristic length of the loading of a structure built up by the material defined on the RVE. In general, the microstructure within one RVE is so complicated that it cannot be described in complete detail. Therefore, quasi-homogeneous subdomains with known physical properties are reasonably chosen. They are called material phases. The homogenized (upscaled) elastic behavior of the material on the observation scale of the RVE, i.e. the relation between homogeneous deformations acting on the boundary of the RVE and resulting macroscopic (average) stresses, can then be estimated from the elastic behavior of the material phases, their volume fractions within the RVE, their characteristic shapes, and their interactions.

We choose the characteristic length of the RVE such that cortical bone is reasonably represented as two-phase composite material [30]: Fluid-filled, vascular pore space is morphologically approximated by cylindrical inclusions in the extravascular (solid) bone matrix, see Fig. 1(b). The overall constitutive behavior is anisotropic, stemming, on the one hand, from (i) the anisotropic orientation of the pore space [21,59,60], and, on the other hand,

from (ii) the anisotropic constitutive behavior of the extravascular bone matrix [61–63].

3.2. Biologically driven evolution of the vascular porosity

First, we note that the characteristic time of primary mineralization (i.e. of the transformation of unmineralized osteoid laid down by the osteoblasts to mineralized bone tissue) is of the order of days [64–66], whereas mechanobiologically triggered or influenced metabolic processes last months to years [67–69]. I.e. the volume fraction of osteoid as compared to mineralized bone is always negligibly small, and, when focussing on the mathematical modeling of the latter, we can consider the primary mineralization process as instantaneous. Hence, in the time frames considered in the present paper, osteoblasts instantaneously form extravascular bone matrix, which is consistent with the micromechanical representation of cortical bone as a two-phase composite of extravascular bone matrix with vascular pores inbetween. The mechanical behavior of such a material is strongly governed by the phase volume fractions f_i, the definition of which ($f_i = V_i/V_{total}$, with V_i as the volume of species i, and V_{total} as the total volume, $V_{total} = \sum_i V_i$) stipulates that the sum of all volume fractions equals one at all times, i.e.

$$f_{vas} + f_{bm} = 1, \qquad (6)$$

with $f_{vas} = f_{vas}(t)$ as the volume fraction of vascular pore space and $f_{bm} = f_{bm}(t)$ as the volume fraction of extravascular bone matrix. We now seek evaluation of the bone cell concentrations provided by the bone cell population model, $C_i = C_i(t)$, compare Eqs. (1)–(4), in terms of corresponding temporal evolutions of the bone constituent volume fractions. The volume fraction of pore space increases due to actively resorbing osteoclasts and decreases due to active osteoblasts producing extravascular bone, thus

$$\frac{df_{vas}}{dt} = k_{res}C_{OC_a} - k_{form}C_{OB_a}, \qquad (7)$$

with k_{res} as the resorption rate quantifying how much bone is resorbed by active osteoclasts per unit time, and with k_{form} as the formation rate quantifying the amount of bone matrix formed by active osteoblasts per unit time. Resorption and formation rates are considered as time-invariant, intrinsic, and species-specific cell properties. The volume fraction of extravascular bone matrix, in turn, decreases due to bone resorption, and increases due to bone formation, thus

$$\frac{df_{bm}}{dt} = -k_{res}C_{OC_a} + k_{form}C_{OB_a}. \qquad (8)$$

Differentiation of Eq. (6) with respect to time yields $df_{vas}/dt = -df_{bm}/dt$. This requirement is fulfilled, as can be easily shown by comparison of Eqs. (7) and (8). Thus, if the volume fractions are known at a certain point in time, the subsequent temporal evolution of f_{vas} and f_{bm} can be tracked by integration of Eqs. (7) and (8).

3.3. Stiffness homogenization

Considering the aforementioned morphology of the RVE of cortical bone, the homogenized fourth-order stiffness tensor of cortical bone, $\mathbb{C}_{cort}^{hom}$, provided by continuum micromechanics, reads as

$$\mathbb{C}_{cort}^{hom} = \sum_r f_r \mathbb{c}_r : \mathbb{A}_r^{est}, \qquad (9)$$

where $\mathbb{c}_r$ is the microscopic fourth-order stiffness tensor of constituent r, $r = vas, bm$, and $\mathbb{A}_r^{est}$ is the estimate of the corresponding fourth-order strain concentration tensor, relating macroscopic and microscopic second-order strain tensors [58]. $\mathbb{A}_r^{est}$ can be estimated

based on Eshelby's classical matrix-inclusion problem [70,71], by means of the Mori–Tanaka scheme [72,73],

$$\mathbb{A}_r^{est} = \left[\mathbb{I} + \mathbb{P}_r^{bm} : (\mathbb{c}_r - \mathbb{c}_{bm}) \right]^{-1}$$
$$: \left\{ \sum_s f_s \left[\mathbb{I} + \mathbb{P}_s^{bm} : (\mathbb{c}_s - \mathbb{c}_{bm}) \right]^{-1} \right\}^{-1}, \qquad (10)$$

where index r denotes either of the two phases, and the summation over index s includes both of them, $s = vas, bm$. Furthermore, $\mathbb{I}$ is the fourth-order unit tensor with its components defined through the Kronecker delta, $\delta_{ij} = 1$ for $i = j$ and zero otherwise, as $I_{ijkl} = 1/2(\delta_{ik}\delta_{jl} + \delta_{il}\delta_{jk})$, and $\mathbb{P}_r^{bm}$ is the fourth-order Hill-tensor of phase r embedded in a matrix with stiffness $\mathbb{c}_{bm}$. For a detailed explanation how the Hill tensor of a cylindrical phase (such as vascular pore space) is calculated, see [30,74].

Evaluation of Eqs. (9) and (10) requires knowledge of phase volume fractions f_r and phase stiffness tensors $\mathbb{c}_r$. The volume fractions are known from the bone cell population model whereas reasonable choice of the phase stiffness tensors requires some more explanation. The vascular pore space is assumed to be filled with water-like fluid (from a mechanical point of view). In the framework of a micromechanical model of bone poroelasticity Hellmich and Ulm [20] showed that (i) assuming undrained conditions is adequate for physiological conditions with reasonably high loading frequencies, and (ii) considering water-type pore fluid, for undrained conditions, as elastic material with negligible shear stiffness is an appropriate approximation. Thus, the stiffness tensor of the vascular porosity reads

$$\mathbb{c}_{vas} = k_{H_2O}\mathbb{J} + \mu_{H_2O}\mathbb{K}, \qquad (11)$$

with $k_{H_2O} = 2.3$ GPa as the bulk modulus, and $\mu_{H_2O} = 0$ as the shear modulus of water; $\mathbb{J}$ is the volumetric part of the fourth-order unit tensor $\mathbb{I}$, and $\mathbb{K}$ is its deviatoric part, $\mathbb{K} = \mathbb{I} - \mathbb{J}$. The components of $\mathbb{J}$ are defined by $J_{ijkl} = 1/3\delta_{ij}\delta_{kl}$. Still, we also performed all simulations reported in this paper under the assumption of the opposing limit case, that of drained conditions ($k_{H_2O} = \mu_{H_2O} = 0$): None of the simulation results were affected by this change. Hence, the poromechanical state of the vascular pore space is irrelevant for the systems biology-micromechanics interactions reported in this paper.

The stiffness tensor of the extravascular bone matrix, $\mathbb{c}_{bm}$, on the other hand, is defined in the line of Fritsch and Hellmich [21]; based on the ultrasonics tests by Ashman et al. [75] conducted on human femurs, $\mathbb{c}_{bm}$ reads in compressed notation (see Appendix B)

$$\mathbb{c}_{bm} = \begin{pmatrix} 18.5 & 10.3 & 10.4 & 0 & 0 & 0 \\ 10.3 & 20.8 & 11.0 & 0 & 0 & 0 \\ 10.4 & 11.0 & 28.4 & 0 & 0 & 0 \\ 0 & 0 & 0 & 12.9 & 0 & 0 \\ 0 & 0 & 0 & 0 & 11.5 & 0 \\ 0 & 0 & 0 & 0 & 0 & 9.3 \end{pmatrix} \text{GPa}. \qquad (12)$$

3.4. Strain concentration and microscopic strain energy density

The macroscopic stress tensor acting on cortical bone, $\boldsymbol{\Sigma}_{cort}$, is related to the corresponding macroscopic strain tensor, $\mathbf{E}_{cort}$, via the macroscopic stiffness tensor obtained from Eq. (9), through a linear elastic constitutive law,

$$\boldsymbol{\Sigma}_{cort} = \mathbb{C}_{cort}^{hom} : \mathbf{E}_{cort} \Longleftrightarrow \mathbf{E}_{cort} = \left(\mathbb{C}_{cort}^{hom} \right)^{-1} : \boldsymbol{\Sigma}_{cort}. \qquad (13)$$

The strains experienced by the extravascular bone matrix affect the activity of the osteocytes residing in that matrix (see Section 2.2), as well as the osteoblasts located at extravascular pore surfaces (see

Section 2.1). Using the previously described micromechanical model for bone stiffness we can express the strain tensor of the extravascular bone matrix (corresponding to a macroscopic load Σ_{cort}) via the strain concentration tensor $\mathbb{A}_{bm}^{est}$ defined by Eq. (10),

$$\varepsilon_{bm} = \mathbb{A}_{bm}^{est} : \mathbf{E}_{cort} = \mathbb{A}_{bm}^{est} : \left[\left(\mathbb{C}_{cort}^{hom} \right)^{-1} : \Sigma_{cort} \right]. \tag{14}$$

Note that the microscopic strain tensor can be alternatively determined based on stress concentration tensor $\mathbb{B}_{bm}^{est}$, $\mathbb{B}_{bm}^{est} = \mathbb{c}_{bm} : \mathbb{A}_{bm}^{est} : (\mathbb{C}_{cort}^{hom})^{-1}$, through the concentration relation $\sigma_{bm} = \mathbb{B}_{bm}^{est} : \Sigma_{cort}$, and subsequent application of the linear elastic constitutive law on the microscopic observation scale, $\varepsilon_{bm} = (\mathbb{c}_{bm})^{-1} : \sigma_{bm}$.

As introduced in Section 2.1, we consider the microscopic SED as scalar representation of the 3D microscopic strain state driving mechanoregulatory responses. The microscopic SED, experienced by the extravascular bone matrix reads as

$$\Psi_{bm} = \frac{1}{2} \varepsilon_{bm} : \mathbb{c}_{bm} : \varepsilon_{bm}, \tag{15}$$

with ε_{bm} following from micromechanics-based strain concentration, according to Eq. (14). It is one of the key features of this paper that mechanoregulation is considered on the microscopic observation scale of extravascular bone matrix (which hosts the mechanosensing and -transducing osteocytes), rather than on the macroscopic observation scale of cortical bone. The consequences of the observation scale on which mechanosensing is considered, are significant and will be highlighted in Sections 3.5, 3.6, and 4.

Summarizing, the functional argument of mechanoregulatory functions Π_{act,OB_p}^{mech} and $P_{RANKL,\varepsilon_{bm}}$, namely the microscopic SED Ψ_{bm}, has been obtained through a sequence of mean-field homogenization, Eqs. (9) and (10), linear elasticity, Eq. (13), strain concentration, Eq. (14), and a classical relation of continuum mechanics, Eq. (15), which eventually enables us to appropriately transfer the 3D macroscopic loading state to a corresponding scalar quantity representing the local strain state of the extravascular bone matrix, see Fig. 1(c) for a schematic sketch of the mechanoregulatory feedback.

3.5. Porosity-dependent micro–macro strain relations

It is evident from Eq. (14) that the strain concentration tensor $\mathbb{A}_{bm}^{est}$ solely governs the difference between macro- and microscopic strain states. For the special case of zero vascular porosity ($f_{vas} = 0$) the macroscopic and microscopic strain states are identical. However, for physiologically observed vascular porosities ($f_{vas} > 0$), ε_{bm} and $\mathbf{E}_{cort}$ significantly deviate from each other. In the following, this f_{vas}-dependent difference between ε_{bm} and $\mathbf{E}_{cort}$ is illustrated through parametric studies, including computation of the components of $\mathbb{A}_{bm}^{est}$, for vascular porosities ranging within $f_{vas} \in [0, 0.5]$, by means of Eqs. (10)–(12). Fig. 3(a) and (b) show the significant non-linearity of $\mathbb{A}_{bm}^{est}$ with respect to f_{vas}. With increasing porosity, the numerical values of the diagonal components of $\mathbb{A}_{bm}^{est}$ (which are equal to one for $f_{vas} = 0$) are decreasing, see Fig. 3(a). The same trend is observed for some of the non-diagonal components of $\mathbb{A}_{bm}^{est}$, see Fig. 3(b), accounting for the morphological change of cortical bone with increasing porosity.

Insertion of these results into Eq. (14) reveals the dependence of ε_{bm} on the corresponding macroscopic strain tensor $\mathbf{E}_{cort}$. To further investigate this dependence numerically, Eq. (14) is evaluated for typical macroscopic strain states, namely for a hydrostatic strain state (represented by strain tensor $\mathbf{E}_{cort}^{hyd}$), and the states of pure shear (represented by strain tensors $\mathbf{E}_{cort}^{shear,12}$, $\mathbf{E}_{cort}^{shear,13}$, and $\mathbf{E}_{cort}^{shear,23}$). The strain tensors are defined as $\mathbf{E}_{cort}^{hyd} = \mathbf{1} \times 10^{-4}$, $\mathbf{E}_{cort}^{shear,12} = (\mathbf{e}_1 \otimes \mathbf{e}_2 + \mathbf{e}_2 \otimes \mathbf{e}_1) \times 10^{-4}$, $\mathbf{E}_{cort}^{shear,13} = (\mathbf{e}_1 \otimes \mathbf{e}_3 + \mathbf{e}_3 \otimes \mathbf{e}_1) \times 10^{-4}$, and $\mathbf{E}_{cort}^{shear,23} = (\mathbf{e}_2 \otimes \mathbf{e}_3 + \mathbf{e}_3 \otimes \mathbf{e}_2) \times 10^{-4}$, with $\mathbf{1}$ as the second-order unit tensor
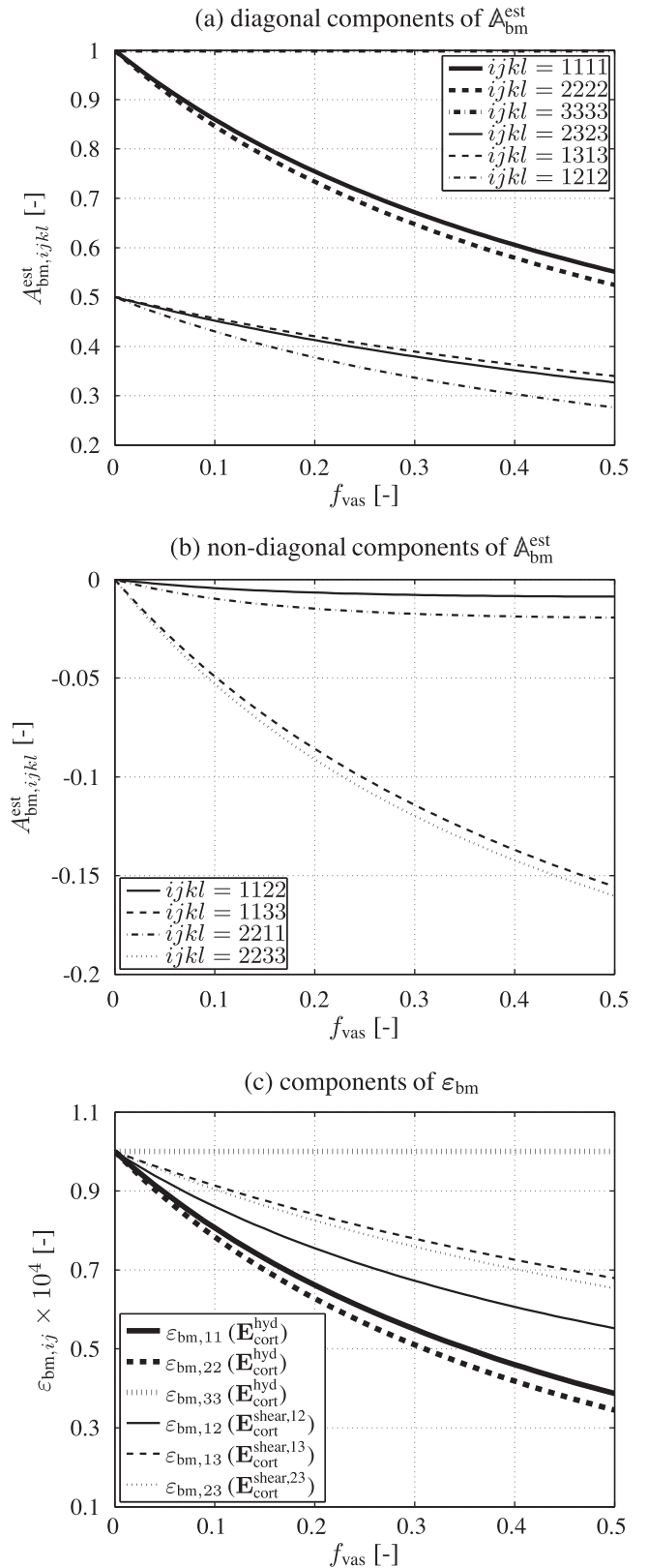

(a) diagonal components of $\mathbb{A}_{bm}^{est}$

(b) non-diagonal components of $\mathbb{A}_{bm}^{est}$

(c) components of ε_{bm}

Fig. 3. Non-zero components of strain concentration tensor $\mathbb{A}_{bm}^{est}$ (with symmetries $A_{bm,ijkl}^{est} = A_{bm,jikl}^{est} = A_{bm,ijlk}^{est} = A_{bm,jilk}^{est}$) as function of vascular porosity f_{vas}, according to Eqs. (10)–(12): (a) diagonal and (b) non-diagonal components $A_{bm,ijkl}^{est}$; (c) components of the symmetric microscopic strain tensor ε_{bm}, according to Eq. (14), evaluated for $\mathbf{E}_{cort}^{hyd}$ (thick graphs), as well as $\mathbf{E}_{cort}^{shear,12}$, $\mathbf{E}_{cort}^{shear,13}$, and $\mathbf{E}_{cort}^{shear,23}$ (thin graphs).

with components δ_{ij} ($\delta_{ij} = 1$ for $i = j$ and zero otherwise), with $\mathbf{e}_1, \mathbf{e}_2$, and $\mathbf{e}_3$ as the unit vectors of a Cartesian coordinate system,

and with symbol $\otimes$ denoting the dyadic product of two vectors. For $\mathbf{E}_{\text{cort}}^{\text{hyd}}$, the strain transfer from the observation scale of cortical bone to the observation scale of extravascular bone matrix differs significantly between the strain tensor components. E.g., for $f_{\text{vas}} = 0.5$, component $E_{\text{cort},33}$ of the macroscopic strain tensor is sensed by the extravascular bone matrix without any attenuation, $\varepsilon_{\text{bm},33} = E_{\text{cort},33}^{\text{hyd}}$, whereas component $E_{\text{cort},22}$ is significantly reduced, $\varepsilon_{\text{bm},22} \approx 0.35 E_{\text{cort},22}^{\text{hyd}}$, see the thick graphs in Fig. 3(c). Thus, a macroscopically hydrostatic strain state is associated with a non-hydrostatic microscopic strain state. Also the strain states of pure shear differ significantly from each other between macro- and microscopic observation scales, see the thin graphs in Fig. 3(c). Except for component $\varepsilon_{\text{bm},33}$, all components of $\boldsymbol{\varepsilon}_{\text{bm}}$ exhibit a striking non-linear dependence with respect to f_{vas} (if the corresponding components of $\mathbf{E}_{\text{cort}}$ are held constant).

The results of the parametric studies presented in this section clearly underpin the importance of estimating the components of the anisotropic strain state that is experienced by the extravascular bone matrix, on the basis of which mechanoregulatory quantities (such as Ψ_{bm}) are computed, by means of a sound multiscale model. The conceptual advantage of a multiscale model over macroscopic models becomes particularly prominent when large porosity ranges have to be considered (as is the case for certain bone disease patterns). It is expected that then macroscopic models fail to appropriately estimate the (porosity-dependent) evolution of microscopic mechanoregulatory quantities following increased or decreased formation of vascular pore space due to bone remodeling events.

3.6. Porosity-dependent micro–macro energy relations

While the parametric studies in Section 3.5 show to which extent the strains occurring on the microscopic observation scale of extravascular bone matrix can deviate from the strains experienced, for exactly the same mechanical loading, on the macroscopic observation scale of cortical bone, the deviation between the microscopic SED, Ψ_{bm}, defined through Eq. (15), and the corresponding macroscopic SED, Ψ_{cort}, defined analogously through $\Psi_{\text{cort}} = (\mathbf{E}_{\text{cort}} : \mathbb{C}_{\text{cort}}^{\text{hom}} : \mathbf{E}_{\text{cort}})/2$, has not been discussed yet. In order to further corroborate the relevance of the multiscale approach proposed in this paper, we will now compare Ψ_{bm} to Ψ_{cort}. To address the question under which circumstances the difference between Ψ_{bm} and Ψ_{cort} becomes significant, Ψ_{bm} and Ψ_{cort} are computed for porosities ranging within $f_{\text{vas}} = [0, 0.5]$, and for different macroscopic stress states: hydrostatic stress $\Sigma_{\text{cort}}^{\text{hyd}}$, pure shear stress states $\Sigma_{\text{cort}}^{\text{shear},12}$, $\Sigma_{\text{cort}}^{\text{shear},13}$, and $\Sigma_{\text{cort}}^{\text{shear},23}$, all of which are defined analogously to the corresponding strain states discussed in Section 3.5, as well as the state of uniaxial stress $\Sigma_{\text{cort}}^{\text{uni},33} = \Sigma_{\text{cort},33}\mathbf{e}_3 \otimes \mathbf{e}_3$. For each value of f_{vas} the macroscopic stiffness tensor, $\mathbb{C}_{\text{cort}}^{\text{hom}}$, is estimated by means of Eqs. (9)–(12). Based on $\mathbb{C}_{\text{cort}}^{\text{hom}}$ and based on the considered macroscopic stress tensors, whose non-zero components are arbitrarily varied extensively in order to cover a wide range of stress magnitudes, the corresponding macro- and microscopic strain tensors, $\mathbf{E}_{\text{cort}}$ and $\boldsymbol{\varepsilon}_{\text{bm}}$, are determined, via Eqs. (13) and (14). These serve then as basis for calculation of Ψ_{bm} and Ψ_{cort}.

For each of the five considered stress states, the ratio $\Psi_{\text{bm}}/\Psi_{\text{cort}}$ turns out to be constant across all stress magnitudes, see Fig. 4, where stress state-specific $\Psi_{\text{bm}}/\Psi_{\text{cort}}$-curves are depicted as functions of f_{vas}. The graphs in Fig. 4 explicitly show that using Ψ_{cort} as mechanoregulatory control variable instead of Ψ_{bm} may lead, depending on the prevailing stress state, to significant misestimations. This is indicated by $\Psi_{\text{bm}}/\Psi_{\text{cort}} \neq 1$ for $f_{\text{vas}} > 0$. Fig. 4 also reveals that accounting for the porosity-dependent deviation of Ψ_{bm} from Ψ_{cort} by empirically defined laws rather than by a sound mul-
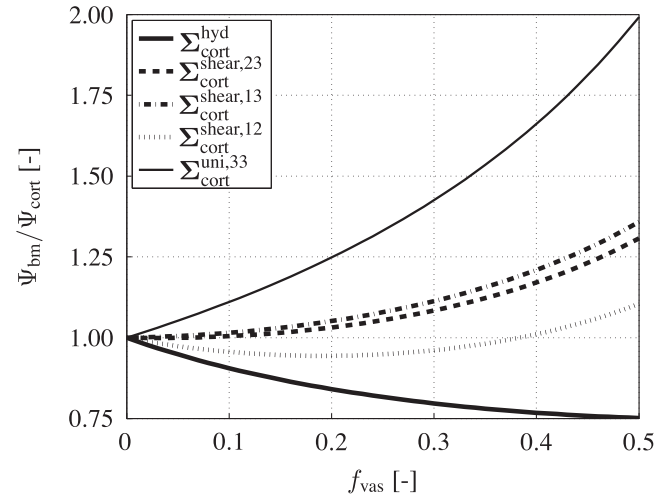

Fig. 4. Ratio $\Psi_{\text{bm}}/\Psi_{\text{cort}}$ as function of the vascular porosity f_{vas}, computed for hydrostatic stress $\Sigma_{\text{cort}}^{\text{hyd}}$, stress states of pure shear $\Sigma_{\text{cort}}^{\text{shear},12}$, $\mathbf{E}_{\text{cort}}^{\text{shear},13}$, and $\Sigma_{\text{cort}}^{\text{shear},23}$, as well as uniaxial stress $\Sigma_{\text{cort}}^{\text{uni},33}$.

tiscale model is a source of potentially severe errors, due to the additional dependence of Ψ_{bm} on the prevailing stress state (compare the distinctively different trends of $\Psi_{\text{bm}}/\Psi_{\text{cort}}$ for $\Sigma_{\text{cort}}^{\text{hyd}}$ and $\Sigma_{\text{cort}}^{\text{uni},33}$, or the somewhat unexpected trend of $\Psi_{\text{bm}}/\Psi_{\text{cort}}$ for $\Sigma_{\text{cort}}^{\text{shear},12}$ with $\Psi_{\text{bm}} \leqslant \Psi_{\text{cort}}$ for $0 \leqslant f_{\text{vas}} \leqslant 0.38$ and $\Psi_{\text{bm}} > \Psi_{\text{cort}}$ otherwise).

4. Significance of mechanoregulation in postmenopausal osteoporosis

Postmenopausal osteoporosis (PMO) is a bone disease eventually leading to an adverse increase of the bone porosity over time which implies a higher fracture risk. According to experimental observations on the pathophysiology of PMO, the disease is accompanied by significant changes within the RANK-RANKL-OPG system. Lemaire et al. [24] suggested that these changes can be (computationally) driven in simplified fashion by prescription of excess PTH. In this section, we investigate the effects of the mechanical feedback on the progress of PMO, with PMO being induced via dosage term $P_{\text{PTH,PMO}} = 5 \times 10^4$ pM/day, see Appendix A for how $P_{\text{PTH,PMO}}$ is mathematically considered in the bone cell population model.

In the following, we will study several scenarios in all of which production of additional PTH is initiated at $t = 0$. To this end, computational simulations are performed, based on the following parameters (if not explicitly defined differently):

- The initial volume fraction of vascular pore space f_{vas}, relating to healthy cortical bone, is set to $f_{\text{vas,ini}} = 0.05$, thus $f_{\text{bm,ini}} = 1 - 0.05 = 0.95$, compare Eq. (6).
- A constant loading of the RVE of cortical bone is prescribed, $\Sigma_{\text{cort},ij}^{\text{normal}} = -30$ MPa if $ij = 33$, and zero otherwise.
- For calibration of the maximum proliferation rate, $\mathcal{P}_{\text{OB}_p}$, we compare the steady state of the preosteoblast evolution, Eq. (1),

$$\mathcal{D}_{\text{OB}_u}C_{\text{OB}_u}\pi_{\text{act,OB}_u}^{\text{TGF-}\beta} + \mathcal{P}_{\text{OB}_p}C_{\text{OB}_p}\breve{\Pi}_{\text{act,OB}_p}^{\text{mech}} - \mathcal{D}_{\text{OB}_p}C_{\text{OB}_p}\pi_{\text{rep,OB}_p}^{\text{TGF-}\beta} = 0,$$

with the corresponding steady state related to the original model disregarding mechanosensing, see [25],

$$\mathcal{D}_{\text{OB}_u}^{\text{Pivonka}}C_{\text{OB}_u}\pi_{\text{act,OB}_u}^{\text{TGF-}\beta} - \mathcal{D}_{\text{OB}_p}C_{\text{OB}_p}\pi_{\text{rep,OB}_p}^{\text{TGF-}\beta} = 0,$$

with $\mathcal{D}_{\text{OB}_u}^{\text{Pivonka}}$ as the maximum differentiation rate of osteoblast progenitor cells, as calibrated by Pivonka et al. [25]. Since both

above equations, for the considered steady state, describe zero gain/loss of the preosteoblast concentration, we can equate them, and so straightforwardly derive an equation for calibration of $\mathcal{P}_{OB_p}$,

$$\mathcal{P}_{OB_p} = \frac{\mathcal{D}_{OB_u}^{Pivonka} C_{OB_u} \pi_{act,OB_u}^{TGF-\beta}}{C_{OB_p} \breve{\Pi}_{act,OB_p}^{mech}} a_{\mathcal{P}_{OB_p}}. \quad (16)$$

Factor $a_{\mathcal{P}_{OB_p}}$, in the sequel called "preosteoblastic proliferation fraction" allows us to prescribe the fraction of preosteoblast gain by proliferation to preosteoblast gain by differentiation, $\mathcal{D}_{OB_u} = (1 - a_{\mathcal{P}_{OB_p}})\mathcal{D}_{OB_u}^{Pivonka}$. Considering physiologically normal conditions, we assign, for provision of new preosteoblasts, a minor fraction to proliferation, $a_{\mathcal{P}_{OB_p}} = 0.1$; nevertheless, this minor fraction turns out to play a significant role, as discussed in Section 6 (see also Fig. 8), see also reference [76].

• The numerical values of all as yet not defined parameters can be found in Appendix A.

Note that Section 6 is devoted to studying variations of above defined parameters.

A number of PMO-scenarios is studied subsequently: Scenario 1 represents non-mechanoresponsive osteoblast proliferation ($\lambda = 0$), scenario 2 represents highly mechanoresponsive osteoblast proliferation ($\lambda = 25$), while scenario 3 represents moderately mechanoresponsive osteoblast proliferation ($\lambda = 1.25$). In scenario 1, where the mechanoregulatory feedback is switched off by setting $\lambda = 0$, implying that the osteoblast proliferation term, see Eq. (1), cannot counteract the catabolic effects of additional production of PTH, bone resorption response is unbounded, see Fig. 5. After a new, disease-related steady state of bone cell concentrations is reached, f_{bm} decreases linearly with time. Maintaining the additional, PMO-related PTH-production long enough would eventually lead to a negative bone matrix volume fraction. Clearly, such a response is neither physiological nor physically reasonable, and underlines the importance of activating the mechanical feedback for simulation of bone remodeling.

In scenario 2, with $\lambda > 0$, the mechanobiological feedback coupling is activated. Directly after initiation of the additional PTH-production, initiated at $t = 0$, a steep increase of f_{vas} is observed. This rapid bone loss leads to a strong increase of the microscopic SED which switches on mechanoregulation, $\Pi_{act,OB_p}^{mech} > \breve{\Pi}_{act,OB_p}^{mech}$, leading to increased proliferation of osteoblast precursor cells. Consequently, the resorption process is steadily reduced until a new equilibrium between bone resorption and bone formation is reached at $f_{bm} \approx 0.94$, with balanced (but increased) bone turnover, see Fig. 5. The time required to reach the new steady state is less than 100 d. Note that keeping up the PTH-production does not lead to further increase of f_{vas}.

While scenario 2 reflects the influence of the implemented anabolic mechanoregulatory mechanism in a qualitatively plausible way, the proliferation-induced compensation of additional PTH-production occurs much too fast (relative to clinical observations). To induce more realistic model predictions in scenario 3, parameter λ is set to $\lambda = 1.25$. The model predictions are compared to the experimental findings by Bonnet and Ferrari [77], who investigated the bone mass evolution (averaged over the whole skeleton without distinction between different types of bones and without specification of the major features of genetic predisposition) during the lifetime of women. Due to the smeared data acquisition it is not possible to carry out experimental validation in a strict sense which would require individual model re-calibration for different types of bone or for different ethnic groups. Nevertheless, comparison of the experimentally obtained bone loss interpreted in terms of a corresponding evolution of the bone matrix volume fraction with the computational results shows that, at least qualitatively, the model adequately resembles the *in vivo* observed porosity increase in patients suffering PMO, see Fig. 5.

Tying in with the study presented in Section 3.6, two further scenarios are simulated, aiming at revealing how the computational results are changed if the mechanical feedback is introduced using the macroscopic SED. Scenario 4 is based on macroscopically controlled mechanoregulation, i.e. in Eq. (2) Ψ_{bm} is substituted by Ψ_{cort}, with $\lambda = 1.25$ and with Ψ_{cort} estimated on the basis of the actual macroscopic bone stiffness, $\mathbb{C}_{cort}^{hom} = \mathbb{C}_{cort}^{hom}(f_{vas}, f_{bm} = 1 - f_{vas})$ according to Eq. (9). Scenario 5 investigates the impact of not updating $\mathbb{C}_{cort}^{hom}$ based on the changing bone constituent volume fractions, thus $\mathbb{C}_{cort}^{hom} = \mathbb{C}_{cort}^{hom}(t = 0) = \mathbb{C}_{cort}^{hom}[f_{vas}(t = 0), f_{bm}(t = 0) = 1 - f_{vas}(t = 0)]$. The computed evolutions of f_{bm} reconfirm that considering Ψ_{cort} instead of Ψ_{bm} as mechanoregulatory argument leads to significant misestimation of the mechanoregulatory response, even if the stiffness of bone is continuously updated, compare the graphs in Fig. 5 representing scenarios 3 and 4. This behavior stems from the different extent of osteoblast proliferation between the microscopic and macroscopic approaches. In the present study, for $f_{vas} > 0$ the numerical value of Ψ_{bm} is higher than the numerical value of Ψ_{cort} (compare Fig. 4) and provokes thus a higher numerical value of Π_{act,OB_p}^{mech} via Eq. (2), leading to a higher concentration of active osteoblasts via Eq. (1) and thus to more bone formation via Eq. (8), which eventually implies faster "interception" of the biochemically induced catabolic regime. Furthermore, the f_{bm}-evolution obtained for scenario 5 clearly shows the importance of a sound estimation tool for the porosity-dependent macroscopic stiffness tensor, see Fig. 5. Neglecting the stiffness decrease due to the biochemically induced porosity increase implies disabling the mechanoresponsiveness of osteoblast proliferation, thus coinciding with scenario 1 ($\lambda = 0$).

5. Significance of mechanoregulation in microgravity-induced disuse

Now, the model response to mechanical disuse and reuse is investigated: Normal loading is again specified by $\Sigma_{cort,ij}^{normal} = -30$ MPa if $ij = 33$ and zero otherwise, and a disuse loading regime is simulated with $\Sigma_{cort,33}^{disuse} = -25$ MPa for $0 \leqslant t \leqslant 2000$ d (after disuse the loading is set back to $\Sigma_{cort,33}^{normal}$ and the system is
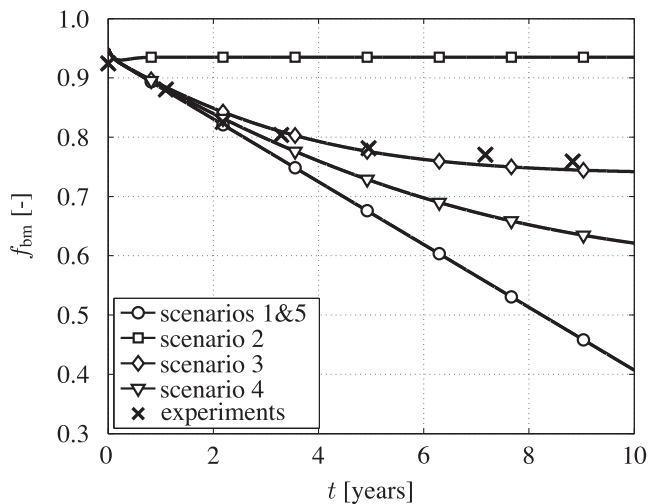

Fig. 5. Numerical simulation of the temporal evolutions of the bone matrix volume fractions, f_{bm}, for five scenarios and comparison with experimental findings by Bonnet and Ferrari [77]; scenario 1: $\lambda = 0$, scenario 2: $\lambda = 25$, and scenario 3: $\lambda = 1.25$ (scenarios 1–3 are based on Ψ_{bm} as control variable for mechanoregulation); scenario 4: $\lambda = 1.25$ and Ψ_{cort} is used as control variable for mechanoregulation; scenario 5: $\lambda = 1.25$, Ψ_{cort} is used as control variable for mechanoregulation, and $\mathbb{C}_{cort}^{hom} = \mathbb{C}_{cort}^{hom}(t = 0) = \mathbb{C}_{cort}^{hom}[f_{vas}(t = 0), f_{bm}(t = 0) = 1 - f_{vas}(t = 0)]$.
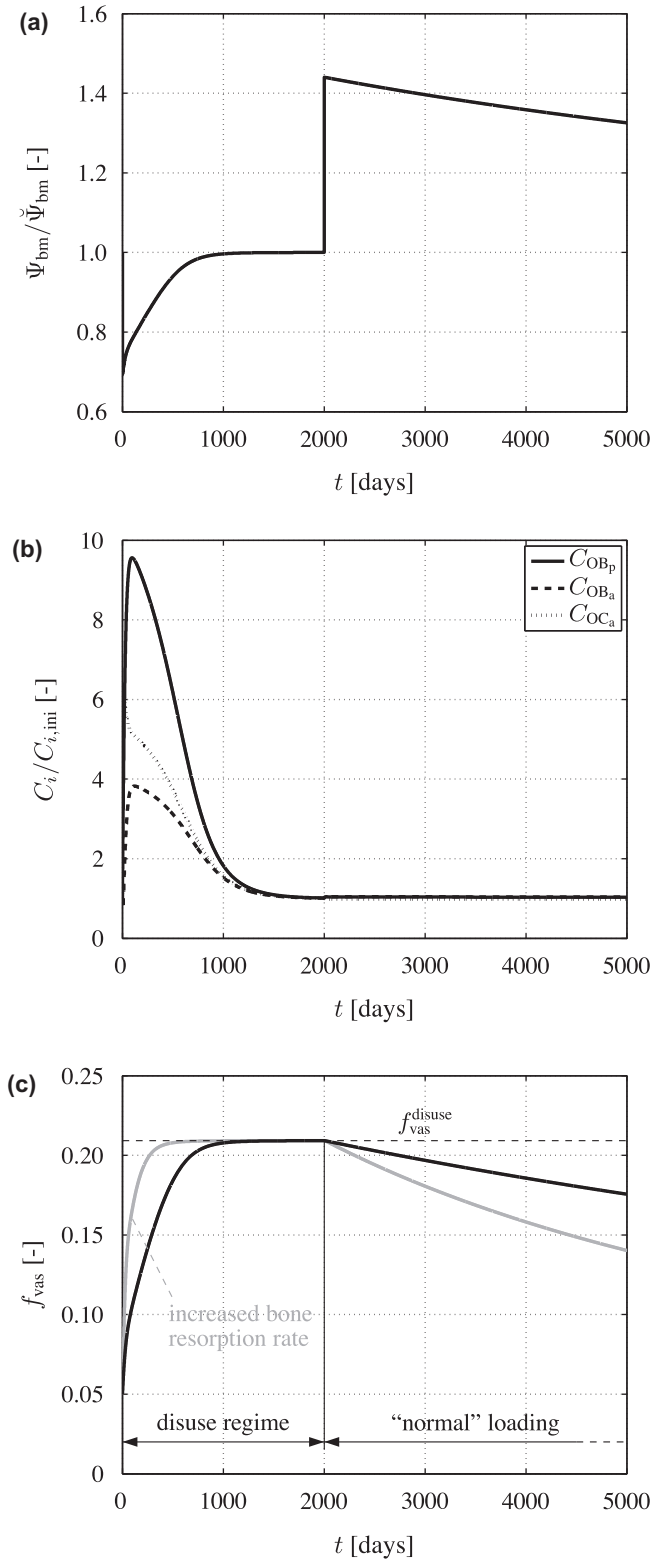
S. Scheiner et al./Comput. Methods Appl. Mech. Engrg. 254 (2013) 181–196

189

Fig. 6. Numerical results for a disuse-scenario, characterized by $\Sigma_{\text{cort},33} = \Sigma_{\text{cort},33}^{\text{disuse}} = -25$ MPa for $0 \leqslant t \leqslant 2000$ d, by and $\Sigma_{\text{cort},33} = \Sigma_{\text{cort},33}^{\text{normal}} = -30$ MPa for $t > 2000$ d; $\kappa = 10^5$ pM/day: evolutions of (a) microscopic strain energy density Ψ_{bm}, normalized with respect to $\breve{\Psi}_{\text{bm}}$, (b) bone cell concentrations C_i, normalized with respect to the initial cell concentrations $C_{i,\text{ini}}$, and (c) vascular porosity f_{vas} for $k_{\text{res}} = 200$ pM^{-1} day^{-1} (black graph) and $k_{\text{res}} = 500$ pM^{-1} day^{-1} (grey graph).

observed for further 3000 d). Inhibition parameter κ, see Eq. (5) and Fig. 2(b), decisively influencing the catabolic model response to a disuse scenario, is set to $\kappa = 10^5$ pM/day – this value has turned out to allow for adequate simulation of bone loss due to decreased mechanical loading. Furthermore, we choose to set $f_{\text{vas,ini}} = 0.05, \lambda = 1.25, a_{\mathcal{P}_{\text{OB}_p}} = 0.1$, and $\breve{\Pi}_{\text{act,OB}_p}^{\text{mech}} = 0.5$; see Section 6 for studies on variations of these parameters.

Evaluating the model accordingly leads, after initiation of the disuse scenario at $t = 0$, to a corresponding drop of the microscopic strain energy density, Ψ_{bm}, see Fig. 6(a). This deviation from the initial loading conditions ($\Psi_{\text{bm}} < \breve{\Psi}_{\text{bm}}$) leads to additional production of RANKL via Eq. (5), initiating a catabolic remodeling regime with $(C_{\text{OC}_a}/C_{\text{OC}_a,\text{ini}}) > (C_{\text{OB}_a}/C_{\text{OB}_a,\text{ini}})$, see Fig. 6(b). Amplification of the osteoclast activity entails a corresponding increase of the volume fraction of vascular pore space, obtained through Eq. (7), see Fig. 6(c). This increase leads to softening of the RVE of cortical bone; i.e. the macroscopic stiffness, accessible via Eqs. (9)–(12), decreases. As the prescribed macroscopic loading $\Sigma_{\text{cort}}^{\text{disuse}}$ is assumed to be constant, decreasing stiffness leads to increasing deformation, and thus to an increasing SED, following Eqs. (13) and (14). Over time, the coupled model approaches a new steady state, with equilibrated bone turnover ($k_{\text{res}}C_{\text{OC}_a} = k_{\text{form}}C_{\text{OB}_a}$) corresponding to adaption of the bone constituent volume fractions to the mechanical disuse. This is observed after ≈ 1000 d, indicated by an afterwards constant volume fraction of vascular pore space, see the black graph in Fig. 6(c), by an equilibrated SED ($\Psi_{\text{bm}} = \breve{\Psi}_{\text{bm}}$), see Fig. 6(a), which results in "shutting off" the disuse-related additional production of RANKL, and consequently by decrease of the cell concentrations to the initial level ($C_i/C_{i,\text{ini}} = 1$), see Fig. 6(b).

After returning to the original macroscopic load at $t = 2000$ d, $\Sigma_{\text{cort},33} = \Sigma_{\text{cort},33}^{\text{normal}}$, deformation increases abruptly (thus $\Psi_{\text{bm}} > \breve{\Psi}_{\text{bm}}$), leading to activation of increased preosteoblast proliferation via Eq. (2). The chosen time frame of 5000 d is however too short to capture the return to the original mechanical steady state (with $f_{\text{vas}} = f_{\text{vas,ini}} = 0.05$). In qualitative terms, the results indicated by the black graphs in Fig. 6 clearly resemble the mechanoregulatory behavior observed for bone subjected to disuse scenarios, compare e.g. the investigations of Vico and co-workers during and after space flight [68,78]. In essence, exposure to microgravity, entailing a reduced loading acting upon bone, leads to adaption of bone mass towards a new equilibrium after a certain period of time. When subjected again to terrestrial gravity, bone responses by recovering, i.e. by adjusting its mass to the original level. Interpreted in terms of bone constituent volume fractions, this is exactly the behavior predicted by the above simulation, see Fig. 6.

Comparison of the model predictions with experimental results shows the importance of thorough species-dependent model calibration. E.g. measurements conducted on cosmonauts after a six month-exposure to microgravity [68] shows a loss of the bone mineral density in cortical bone of not more than 2.5% (observed in the distal radius) and 4.3% (observed in the distal tibia), respectively. I.e. the experimentally observed average bone loss rate amounted to 0.42%/month (distal radius) and 0.72%/month (distal tibia), respectively. The computationally predicted bone loss rate, 0.48%/month, see the black graph in Fig. 6(c), fits well for this experimental data range. On the other hand, microgravity experiments on other species, e.g. on rats [78], showed much higher bone loss rates. Most likely, this more responsive behavior can be assigned to a species-dependent, increased resorption activity of active osteoclasts. To highlight this effect, a second disuse-study is carried out, with the resorption (and also the formation) rate being increased by factor 2.5, i.e. $k_{\text{res}} = 500$ (pM day)$^{-1}$. The grey graph in Fig. 6(c) shows that this measure leads to a dramatic acceleration of the resorption response, with mechanical adaption being fin-

ished much faster. Hence, the model response can be adjusted to different species (and bone tissues), by adjustment of the underlying parameters. However, the focus of this paper is not on re-calibrating the bone cell population model, but on highlighting the capabilities of the mechanoregulatory mechanisms introduced in Sections 2.1 and 2.2 – the former endeavor is thus not further pursued in this paper.

6. Sensitivities of the mechanoregulatory parameters

In the following, the sensitivity of the model output to variations of single parameters is investigated. If not explicitly specified differently, model parameters are chosen as defined in Sections 4 and 5.

Investigation of inhibition parameter κ and of anabolic strength parameter λ: First, the sensitivity of the computed bone constituent volume fractions to the parameters governing the mechanoresponsiveness of the model, i.e. to the inhibition parameter κ and to the anabolic strength parameter λ, is investigated. Parameter κ governs the maximum, mechanically induced "external" dose of RANKL, see Eq. (5). The model is evaluated for four values of κ, $\kappa_1 = 10^2$ pM/day, $\kappa_2 = 10^{3.5}$ pM/day, $\kappa_3 = 10^{4.5}$ pM/day, and $\kappa_4 = 10^6$ pM/day. As anticipated, a low value of κ induces a slow increase of f_{vas} during disuse, due to the weak additional, disuse-related stimulation of osteoclast differentiation. Increasing κ leads to much faster bone loss, thus the disuse-related steady state composition (see Section 5 for a detailed discussion) is also approached faster, see the graphs in the dark grey area in Fig. 7. The capacity of the RANK-RANKL-OPG system to promote the differentiation of osteoclasts is however limited, i.e. further increase of κ, e.g. $\kappa \gg \kappa_4$, does not yield a corresponding increase of the slope of $f_{vas}(t)$ in the disuse regime. Hence, further acceleration of the catabolic response to disuse cannot be achieved by increasing κ.

The sensitivity of increased osteoblast proliferation to increased loading, on the other hand, is controlled by parameter λ, see Eq. (2). The recovery of the vascular porosity, after switching off disuse, towards the original value at $t = 0$ (again, see Section 5 for a detailed discussion of disuse–reuse-scenarios) can be accelerated by increasing λ, see the graphs in the light grey area in Fig. 7, obtained through evaluation of the model for $\lambda_1 = 1, \lambda_2 = 2, \lambda_3 = 4$, and $\lambda_4 = 10$. Due to reaching the upper limit of
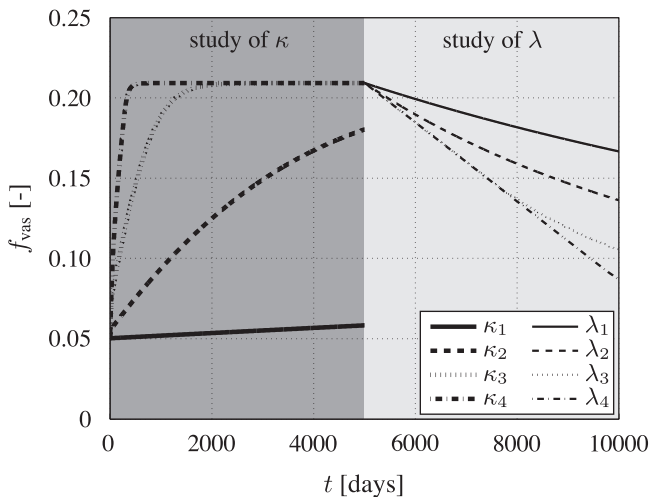

Fig. 7. Sensitivity of f_{vas} to κ and λ, according to Eqs. (2) and (5), with $\kappa_1 = 10^2$ pM d^{-1}, $\kappa_2 = 10^{3.5}$ pM/day, $\kappa_3 = 10^{4.5}$ pM/day, and $\kappa_4 = 10^6$ pM/day (and $\lambda = 25$), as well as $\lambda_1 = 1, \lambda_2 = 2, \lambda_3 = 4$, and $\lambda_4 = 10$ (and $\kappa = 10^5$ pM/day); the dark/light grey area indicates the time frame for which results of the κ-/λ-study are presented.
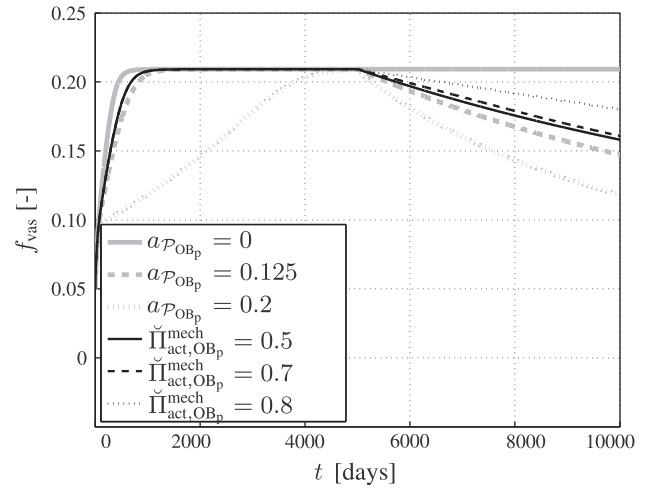

Fig. 8. Sensitivity of f_{vas} to parameters $a_{\mathcal{P}_{OB_p}}$ and $\breve{\Pi}^{mech}_{act,OB_p}$, governing the extent and flexibility of osteoblast proliferation; grey/black lines indicate varying values of $a_{\mathcal{P}_{OB_p}}$ (with $\breve{\Pi}^{mech}_{act,OB_p} = 0.5$) and $\breve{\Pi}^{mech}_{act,OB_p}$ (with $a_{\mathcal{P}_{OB_p}} = 0.1$).

Π^{mech}_{act,OB_p}, max $\Pi^{mech}_{act,OB_p} = 1$ (see Fig. 2), the anabolic capacity of osteoblast proliferation is limited, thus choosing $\lambda \gg \lambda_4$ does not lead to a correspondingly faster re-establishment of $f_{vas,ini}$ (see e.g. the initially coinciding slopes of the graphs related to λ_3 and λ_4 in the light grey area in Fig. 7).

Investigation of preosteoblastic proliferation fraction $a_{\mathcal{P}_{OB_p}}$ and of the minimum value of the preosteoblast activator function Π^{mech}_{act,OB_p}: The second study is devoted to examining the role of the parameters that are central for calibration of proliferation rate $\mathcal{P}_{OB_p}$, $a_{\mathcal{P}_{OB_p}}$ and $\breve{\Pi}^{mech}_{act,OB_p}$, see Eq. (16). Factor $a_{\mathcal{P}_{OB_p}}$ controls how many osteoblast precursors are supplied by differentiation of osteoblast progenitors, and how many by proliferation of osteoblast precursors. The minimum value of the preosteoblast proliferation activator function Π^{mech}_{act,OB_p} at steady-state conditions, $\breve{\Pi}^{mech}_{act,OB_p}$, determines the capacity to induce mechanically triggered bone formation. The simulations, carried out for $a_{\mathcal{P}_{OB_p}} = \{0, 0.125, 0.2\}$ and $\breve{\Pi}^{mech}_{act,OB_p} = \{0.5, 0.7, 0.8\}$ show that increasing $a_{\mathcal{P}_{OB_p}}$ leads to deceleration of bone resorption during disuse, and to acceleration of bone formation during recovery from disuse, see Fig. 8. While varying $\breve{\Pi}^{mech}_{act,OB_p}$ has no influence whatsoever on bone resorption, increasing $\breve{\Pi}^{mech}_{act,OB_p}$ leads to slowing down bone formation, due to narrowing down the margin between $\breve{\Pi}^{mech}_{act,OB_p}$ and max $\Pi^{mech}_{act,OB_p} = 1$, see also Fig. 2(a). Decreasing $\breve{\Pi}^{mech}_{act,OB_p}$ below 0.5 becomes only relevant for a significantly increased loading. However, such substantial load increase can be considered as physiologically implausible and is thus not investigated here.

The results depicted in Figs. 7 and 8 also illustrate that both the slopes of a catabolic regime (with $df_{vas}/dt > 0$) and of an anabolic regime (with $df_{vas}/dt < 0$) are bounded by a certain limiting value. A further study (not presented in this paper) of the combined effect of κ and $a_{\mathcal{P}_{OB_p}}$ on the time span after which the disuse-related "steady state" porosity is reached shows that, for the given mechanical loading regime, the lower limit of completed catabolic mechanical adaption is ≈ 270 d, corresponding to an average bone loss rate of 1.81%/month (if k_{res} is not increased as shown in Section 5). Increasing the responsiveness of the system, beyond this limit, thus requires incorporation of additional (biochemical) mechanoregulatory mechanisms, allowing to further increase ratios C_{OC_a}/C_{OB_a} (during disuse) and C_{OB_a}/C_{OC_a} (during overuse), respectively.

Investigation of initial porosity $f_{vas,ini}$ and of loading magnitude $\Sigma^{disuse}_{cort,33}$: The analysis so far has demonstrated how porosity increase
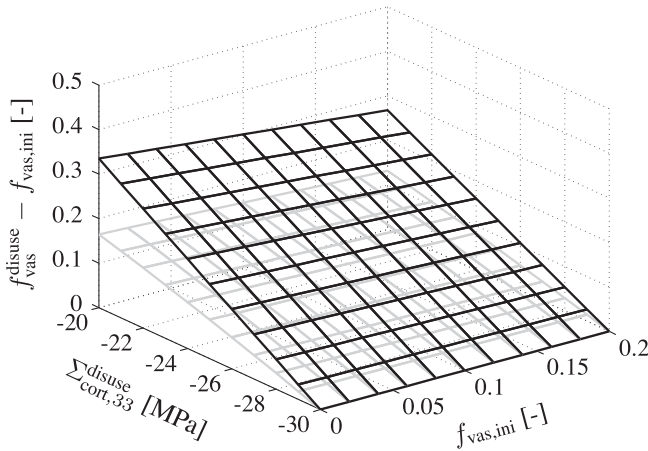
S. Scheiner et al./Comput. Methods Appl. Mech. Engrg. 254 (2013) 181–196

191

Fig. 9. The porosity relating to the disuse steady state, $f_{\mathrm{vas}}^{\mathrm{disuse}}$, as function of the initial porosity, $f_{\mathrm{vas,ini}}$, and of the 33-component of the macroscopic stress tensor during disuse, $\Sigma_{\mathrm{cort,33}}^{\mathrm{disuse}}$; simulations are carried out for two stress tensors representing normal loading, $\Sigma_{\mathrm{cort}}^{\mathrm{normal,uni}} = [0,0,0;0,0,0;0,0,-30]$ MPa (black graph) and $\Sigma_{\mathrm{cort}}^{\mathrm{normal,3D}} = [4,2,7;2,-10,-3;7,-3,-30]$ MPa (grey graph).

and decrease are influenced by the underlying parameters, $\kappa, \lambda, a_{\mathcal{P}_{\mathrm{OB_p}}}$, and $\breve{\Pi}_{\mathrm{act,OB_p}}^{\mathrm{mech}}$. The disuse-related steady state value of $f_{\mathrm{vas}}, f_{\mathrm{vas}}^{\mathrm{disuse}}$, has turned out to be not affected by variations of those parameters, with $f_{\mathrm{vas}}^{\mathrm{disuse}} \approx 0.21$. In the last study of this section, the parameters for which $f_{\mathrm{vas}}^{\mathrm{disuse}}$ is sensitive are investigated: the initial volume fraction of the vascular porosity, $f_{\mathrm{vas,ini}}$; the magnitude of disuse, e.g. $\Sigma_{\mathrm{cort,33}}^{\mathrm{disuse}}$ for uniaxial loading; and the direction of the applied loading. In detail, simulations are performed for $f_{\mathrm{vas,ini}} = [0,0.2]$, for $\Sigma_{\mathrm{cort,33}}^{\mathrm{disuse}} = [-30,-25]$ MPa, and for two different macroscopic stress tensors representing normal loading, namely uniaxial compression $\Sigma_{\mathrm{cort}}^{\mathrm{normal,uni}} = [0,0,0;0,0,0;0,0,-30]$ MPa, and a general three-dimensional stress state $\Sigma_{\mathrm{cort}}^{\mathrm{normal,3D}} = [4,2,7;2,-10,-3;7,-3,-30]$ MPa. The simulations show that the maximum porosity increase during disuse, $f_{\mathrm{vas}}^{\mathrm{disuse}} - f_{\mathrm{vas,ini}}$, decreases with increasing $f_{\mathrm{vas,ini}}$ and with increasing $\Sigma_{\mathrm{cort,33}}^{\mathrm{disuse}}$ (and thus with increasing $|\Sigma_{\mathrm{cort,33}}^{\mathrm{normal}} - \Sigma_{\mathrm{cort,33}}^{\mathrm{disuse}}|$), see Fig. 9. Furthermore, the distinctive difference between the black graph (representing the results for $\Sigma_{\mathrm{cort}}^{\mathrm{normal,uni}}$) and the grey graph (representing the results for $\Sigma_{\mathrm{cort}}^{\mathrm{normal,3D}}$) highlights that not only a simplified scalar variation (e.g. of the stress in the main load direction) but the component-wise change of the 3D stress tensor has to be considered for profound prediction of mechanical adaption of bone. This behavior conforms with experimental observations that different parts of bone, subjected to different stress states, exhibit different bone remodeling responses to mechanical stimuli [79]. In more detail, Carter [79] states that *"the magnitudes, orientations, and sense (tension or compression) of [...] strains vary markedly throughout the skeleton. It is probable, therefore, that the strain/ remodeling response of bone is site specific"*. Variations in strain/ remodeling response due to variations in magnitude and orientation of strains applied onto cortical bone are reflected in the difference between black and grey graphs in Fig. 7.

7. Discussion of potentials and limitations of the presented approach

In the presented approach, one single value $\breve{\Psi}_{\mathrm{bm}}$ of the strain energy density relating to a bone turnover in equilibrium is chosen. This is still reminiscent of the approach of Beaupré et al. [80], where, below an attractor state strain energy density Ψ_{AS}, tissue resorption is triggered, and at strain energies exceeding this state, bone tissue is laid down. In our approach, the mechanical strains

(still quantified in terms of the strain energy density) are directly related to biochemical and biological events as recorded in systems biology, and the latter, through a cascade of events which we model in a reductionist fashion, finally lead to bone formation or resorption. In more detail, we introduce into our model two distinct pathways, one catabolic and one anabolic one, which – when acting together – form something comparative to a regulatory mechanism. This we regard as an original feature of our model, incorporating explicitly system biological features into the mechanoregulatory loop. Still, our variable $\breve{\Psi}_{\mathrm{bm}}$ takes somehow the role of the attractor state – though, in principal, it may well be different for anabolic and catabolic events. The more precise identification of strain thresholds beyond or within which biochemical events are recorded is a very fascinating topic, which we plan to look into in the near future.

The illustrative examples given in the previous sections refer to physiologically normal as well as to reduced loading conditions. The use of the presented model for cases of overloading may be questionable since phenomena such as microdamage growth are not explicitly accounted for. Respective mechanobiological formulations, covering also events of "stress fractures", have been proposed [81,82]. While McNamara and Prendergast [82] do not distinguish between porosity- and damage-driven stiffness reduction, García-Aznar et al. [81] adopt in their approach classical damage mechanics, based on a scalar damage variable which is still not directly related to the cortical microstructure. As interesting conceptual alternative, our present micromechanical approach may be conceptually extended towards the introduction of microcracks as an additional material phase [83,84]. As for propagation of cracks, which could finally lead to fatigue failure, the number of load cycles would appear as a very important model parameter, which would drive crack propagation, and therefore increase the stress or strain states experienced by the osteocytes. In other words, *load history* would become an important factor as "mechanical stimulus". This is conceptually similar to the stimulus variables accounting for load cycles, as introduced by Carter and colleagues in the 1980's [85,86]. These aspects are beyond the scope of the present contribution, marking a clear limitation of the present approach.

We note that the micromechanical representation in Fig. 1(b) does not represent the entirety of cortical microstructural features, such as the branching network of Haversian systems [87], also referred to as Haversian and Volkmann's canals [88]. However, the chosen degree of abstraction (i.e. cylinders instead of oriented branches) still allows for satisfactory prediction of vascular porosity-dependent elastic properties, as was shown in numerous published works over more than 30 years, including [59,89–97].

8. Conclusions

The presented methodology provides biophysically reasonable estimates of the stiffness changes of cortical bone (and thus of its load-carrying capacity), driven by biochemically and/or mechanically regulated bone cell activities. This is achieved through coupling of a bone cell population model with a continuum micromechanics model of bone stiffness, via a strain energy density-based feedback loop implemented on the observation scale of extravascular bone matrix, which controls both bone resorption and bone formation responses. The implemented approach involves a number of notable original aspects: (i) for the first time, state-of-the-art models of bone biology and bone mechanics are fully coupled; (ii) osteoblast proliferation is taken into account, based on experimental evidence, governed by the prevailing mechanical loading; (iii) production of RANKL is considered as

being modulated by the prevailing mechanical loading, also based on experimental evidence; and (iv) the strain energy density experienced by the extravascular bone matrix (i.e. on the observation scale of the relevant cellular events involved in bone remodeling) is used as mechanoregulatory quantity. The performed numerical simulations gave insights into a variety of aspects related to bone remodeling and mechanical feedback control. In particular, the following observations have been made:

- It is essential to consider the microscopic strain energy density, Ψ_{bm}, as functional argument for mechanoregulation, on the observation scale of extravascular bone matrix (which hosts the mechanosensing and -transducing osteocytes).

  The significance of using the microscopic strain energy density, Ψ_{bm}, as functional argument for the proposed mechanoregulatory mechanisms, rather than the macroscopic strain energy density, Ψ_{cort}, has turned out to strongly depend on actual vascular porosity f_{vas} and stress state Σ_{cort}. While for low porosities (i.e., close to zero) Ψ_{cort} and Ψ_{bm} are virtually identical, for higher porosities strong deviations between these quantities are found; particularly for high porosities which might be associated with severe bone loss (such as in cancer or advanced osteoporosis) or in trabecular bone, Ψ_{cort} significantly underestimates Ψ_{bm}.

- Proliferation of osteoblast precursors has been identified as powerful mechanism for modulating bone remodeling towards an anabolic regime. Careful calibration of the involved parameters is crucial. Especially ratio $a_{\mathcal{P}_{OB_p}}$, governing the magnitude of osteoblast proliferation, exerts a major influence on the accuracy of the computed bone remodeling response.

- Simulations of postmenopausal osteoporosis (PMO) showed that using the bone cell population model without consideration of mechanoregulatory feedback leads to continuous, unbounded bone loss. Such behavior is of course not observed *in vivo*. Experiments rather show an initial phase of rapid bone loss followed by a second phase of moderate, decreasing bone loss. An active mechanoregulatory feedback reduces the high bone loss rate observed directly after initiation of PMO and allows for computation of bone volume fraction evolutions over time resembling corresponding experimental results.

- Simulations of a mechanical disuse- and reuse-regime showed that the model is capable of (qualitatively) reproducing physiologically observed key features, such as rapid bone loss due to unloading and slower bone gain after re-establishment of the normal mechanical loading. Calibration of the catabolic mechanoregulatory function via parameter κ allows for adjustment of the time it takes until a new steady state, related to mechanical disuse, is reached. However, the catabolic regulatory function π_{act,OC_p}^{RANKL} which upregulates the differentiation from osteoclast precursors to active osteoclasts is limited, $\pi_{act,OC_p}^{RANKL} = [0,1]$, i.e. increasing of $P_{RANKL,\varepsilon_{bm}}$ beyond a certain limit value does not lead to further acceleration of the corresponding bone resorption response. This limitation can be overcome by modifying the resorption rate of active osteoclasts k_{res}.

The numerical results indicate that the proposed approach captures key features of mechanoregulation of bone remodeling. Nevertheless, several aspects have to be revisited in future research. In particular, (i) explicit introduction of osteocytes and the major signaling pathways between osteocytes and bone-forming/-resorbing cells, and (ii) further improvement of the model as to the different mechanism by which the mechanical loading is sensed, is envisaged to provide new insights on mechanoregulation of bone remodeling, eventually allowing for further experimental validation of the model and utilization as interpretative and predictive instrument.

Appendix A. Functions and parameters governing the bone cell population model

Hereafter, we will briefly present the mathematical framework required to evaluate the governing differential Eqs. (1), (3), and (4); a detailed elaboration can be found in [25,26]. In order to take into account the influence of the biochemical environment on cell differentiation and apoptosis processes, activator and repressor functions are included in the model, defined according to the concept of the so-called Hill functions [98]. The activator and repressor functions related to the influence of TGF-β read

$$\pi_{act,OB_u}^{TGF-\beta} = \frac{C_{TGF-\beta}}{K_{act,OB_u}^{TGF-\beta} + C_{TGF-\beta}}, \tag{A.1}$$

$$\pi_{rep,OB_p}^{TGF-\beta} = \frac{K_{rep,OB_p}^{TGF-\beta}}{K_{rep,OB_p}^{TGF-\beta} + C_{TGF-\beta}}, \tag{A.2}$$

and

$$\pi_{act,OC_a}^{TGF-\beta} = \frac{C_{TGF-\beta}}{K_{act,OC_a}^{TGF-\beta} + C_{TGF-\beta}}, \tag{A.3}$$

with $C_{TGF-\beta}$ as the concentration of TGF-β, and with $K_{act,OB_u}^{TGF-\beta}$, $K_{rep,OB_p}^{TGF-\beta}$, and $K_{act,OC_a}^{TGF-\beta}$ as equilibrium dissociation constants related to the action of TGF-β binding to its receptors on the involved cell types. The actual concentration of TGF-β is based on considering the release of the TGF-β stored in bone during resorption, and application of the principle of mass action kinetics, yielding

$$C_{TGF-\beta} = \frac{\alpha k_{res} C_{OC_a} + S_{TGF-\beta}}{\widetilde{D}_{TGF-\beta}}, \tag{A.4}$$

where α is a constant quantifying the content of TGF-β in the bone matrix, $S_{TGF-\beta}$ is a sink/source term for TGF-β, and $\widetilde{D}_{TGF-\beta}$ is the constant degradation rate of TGF-β.

The activator function related to binding of RANKL to RANK, promoting osteoclast differentiation, is defined as

$$\pi_{act,OC_p}^{RANKL} = \frac{C_{[RANKL-RANK]}}{K_{d,[RANKL-RANK]} + C_{[RANKL-RANK]}}, \tag{A.5}$$

with $C_{[RANKL-RANK]}$ as the concentration of the RANK-RANKL complex, and $K_{d,[RANKL-RANK]}$ as the corresponding equilibrium dissociation binding constant. The former follows from

$$C_{[RANKL-RANK]} = K_{a,[RANKL-RANK]} C_{RANKL} C_{RANK}, \tag{A.6}$$

with $K_{a,[RANKL-RANK]}$ as the equilibrium association binding constant related to binding of RANKL to RANK, C_{RANK} as the concentration of RANK which is defined through a constant production rate intrinsic to osteoclast precursor cells [25,26], and C_{RANKL} as the concentration of RANKL available for combination with RANK found on the membranes of osteoclast precursor cells, turning them into active

osteoclasts. This availability, in turn, is governed by the binding of already produced RANKL through RANK and osteoprotegerin (OPG), the latter being released by osteoblasts, and by the production of RANKL itself,

$$C_{RANKL} = \frac{C_{RANKL}^{max} \frac{\beta_{RANKL} + P_{RANKL}}{\beta_{RANKL} + \widetilde{D}_{RANKL} C_{RANKL}^{max}}}{1 + K_{a,[RANKL\text{-}OPG]} C_{OPG} + K_{a,[RANKL\text{-}RANK]} C_{RANK}}. \tag{A.7}$$

In Eq. (A.7), $K_{a,[RANKL\text{-}OPG]}$ denotes the equilibrium association constant for binding of OPG to RANKL, C_{OPG} is the concentration of OPG (following from the principle of mass action kinetics), β_{RANKL} is the intrinsic RANKL production rate, P_{RANKL} is the ("external") dosage of RANKL, $\widetilde{D}_{RANKL}$ is the constant degradation rate, C_{RANKL}^{max} is the maximum concentration of RANKL (also referred to as effective carrying capacity). C_{RANKL}^{max} is assumed to be regulated by PTH, through the following relation:

$$C_{RANKL}^{max} = \left(N_{RANKL}^{OB_p} C_{OB_p} + N_{RANKL}^{OB_a} C_{OB_a} \right) \pi_{act,OB}^{PTH}, \tag{A.8}$$

where $N_{RANKL}^{OB_p} = N_{RANKL}^{OB_a} = N_{RANKL}^{OB}$ are the maximum numbers of RANKL receptors on osteoblast precursors and active osteoblasts, and $\pi_{act,OB}^{PTH}$ is an activator function related to the presence of PTH, reading

$$\pi_{act,OB}^{PTH} = \frac{C_{PTH}}{K_{act,OB}^{PTH} + C_{PTH}}. \tag{A.9}$$

In Eq. (A.9), $K_{act,OB}^{PTH}$ denotes the RANKL production-relevant equilibrium dissociation constant related to binding of PTH to its receptors expressed on osteoblasts, and C_{PTH} denotes the concentration of PTH, determined by

$$C_{PTH} = \frac{\beta_{PTH} + P_{PTH,d}}{\widetilde{D}_{PTH}}, \tag{A.10}$$

with β_{PTH} as intrinsic PTH production rate, $P_{PTH,d}$ as PTH dosage term, and $\widetilde{D}_{PTH}$ as constant PTH degradation rate.

Furthermore, the expression given by Eq. (A.7) includes the concentration of OPG, which is given by

$$C_{OPG} = \frac{(\beta_{OPG} + P_{OPG,d}) C_{OPG}^{max}}{\beta_{OPG} + \widetilde{D}_{OPG} C_{OPG}^{max}}, \tag{A.11}$$

where β_{OPG} is the intrinsic OPG production rate, $P_{OPG,d}$ is the OPG dosage term, $\widetilde{D}_{OPG}$ is the constant OPG degradation rate, and C_{OPG}^{max} is the maximum OPG concentration. The production rate of OPG, in turn, is also regulated by PTH,

$$\beta_{OPG} = \left(p_{OB_p}^{OPG} C_{OB_p} \pi_{rep,OB}^{PTH} + p_{OB_a}^{OPG} C_{OB_a} \pi_{rep,OB}^{PTH} \right), \tag{A.12}$$

where $p_{OB_p}^{OPG} = p_{OB_a}^{OPG} = p_{OB}^{OPG}$ are proportionality constants quantifying the OPG production of osteoblast precursors and active osteoblasts, and $\pi_{rep,OB}^{PTH}$ is the repressor function related to OPG production if PTH binds to osteoblasts. $\pi_{rep,OB}^{PTH}$ is defined by

$$\pi_{rep,OB}^{PTH} = \frac{K_{rep,OB}^{PTH}}{K_{rep,OB}^{PTH} + C_{PTH}}, \tag{A.13}$$

with $K_{rep,OB}^{PTH}$ denoting the OPG production-relevant equilibrium dissociation constant related to binding of PTH to its receptors expressed on osteoblasts.

Table 1 summarizes the parameters needed for numerical evaluation of the equations presented in this paper, as calibrated in aforementioned papers. The bone formation rate k_{form} is calibrated such that for the previously defined bone resorption rate, k_{res}, steady-state cell concentrations, $dC_{OB_p}/dt = dC_{OB_a}/dt = dC_{OC_a}/dt = 0$,

Table 1
Parameters governing the bone cell population model, defined through Eqs. (1)–(8) and (A.1)–(A.13).

Parameter	Numerical value	Unit
$\mathcal{A}_{OB_a}$	2.1107×10^{-1}	d^{-1}
$\mathcal{A}_{OC_a}$	5.6487×10^{-4}	d^{-1}
C_{OPG}^{max}	2×10^{8}	pM
$\mathcal{D}_{OB_u}^{Pivonka}$	7×10^{-2}	d^{-1}
$\mathcal{D}_{OB_p}$	1.6570×10^{-1}	d^{-1}
$\mathcal{D}_{OC_p}$	2.1×10^{0}	d^{-1}
$\widetilde{D}_{OPG}$	3.5×10^{-1}	d^{-1}
$\widetilde{D}_{PTH}$	8.6×10^{1}	d^{-1}
$\widetilde{D}_{RANKL}$	1.0132×10^{1}	d^{-1}
$\widetilde{D}_{TGF\text{-}\beta}$	1×10^{0}	d^{-1}
k_{res}	2×10^{0}	$(pM\ day)^{-1}$
$K_{act,OB_u}^{TGF\text{-}\beta}$	5.6328×10^{-4}	pM
$K_{act,OB}^{PTH}$	1.5×10^{2}	pM
$K_{act,OC_a}^{TGF\text{-}\beta}$	5.6328×10^{-4}	pM
$K_{d,[RANKL\text{-}RANK]}$	5.6797×10^{0}	pM
$K_{rep,OB}^{PTH}$	2.226×10^{-1}	pM
$K_{rep,OB}^{TGF\text{-}\beta}$	1.7543×10^{-4}	pM
$K_{a,[RANKL\text{-}OPG]}$	1×10^{-3}	pM^{-1}
$K_{a,[RANKL\text{-}RANK]}$	3.4118×10^{-2}	pM^{-1}
N_{RANKL}^{OB}	2.703×10^{6}	–
p_{OB}^{OPG}	1.625×10^{8}	$pM\ d^{-1}$
α	1×10^{-2}	–
β_{PTH}	2.5×10^{2}	$pM\ d^{-1}$
β_{RANKL}	1.6842×10^{2}	$pM\ d^{-1}$

imply a balanced bone turnover; i.e. $f_{vas} = $ const. and $f_{bm} = $ const. in Eqs. (7) and (8): $k_{form} = k_{res} C_{OC_a}/C_{OB_a}$.

Furthermore, the steady state of the bone cell population model follows the work of Pivonka et al. [25], related cell concentrations amount to $C_{OB_u} = 0.01$ pM, $C_{OB_p} = 0.001$ pM, $C_{OB_a} = 0.0005$ pM, $C_{OC_p} = 0.001$ pM, and $C_{OC_a} = 0.0001$ pM. Note that C_{OB_u} and C_{OC_p} are presumed to be constant and hence not state variables of our model.

Appendix B. Tensor notation

For numerical evaluation of equations involving tensor operations, compression of second- and fourth-order tensors, respectively, into equivalent 6×1-vector and 6×6-matrix notations, respectively, has turned out to be useful. This compressed notation is also referred to as Kelvin- or Mandel-notation [99,100]. Accordingly, a symmetric second-order tensor, e.g. strain tensor $\boldsymbol{\varepsilon}$, can be alternatively specified by

$$\boldsymbol{\varepsilon} = \begin{bmatrix} \varepsilon_{11} & \varepsilon_{22} & \varepsilon_{33} & \sqrt{2}\varepsilon_{23} & \sqrt{2}\varepsilon_{13} & \sqrt{2}\varepsilon_{12} \end{bmatrix}^T. \tag{B.14}$$

On the other hand, a symmetric fourth-order tensor, e.g. stiffness tensor $\mathbb{c}$, reads in compressed notation

$$\mathbb{c} = \begin{pmatrix} c_{1111} & c_{1122} & c_{1133} & \sqrt{2}c_{1123} & \sqrt{2}c_{1113} & \sqrt{2}c_{1112} \\ c_{2211} & c_{2222} & c_{2233} & \sqrt{2}c_{2223} & \sqrt{2}c_{2213} & \sqrt{2}c_{2212} \\ c_{3311} & c_{3322} & c_{3333} & \sqrt{2}c_{3323} & \sqrt{2}c_{3313} & \sqrt{2}c_{3312} \\ \sqrt{2}c_{2311} & \sqrt{2}c_{2322} & \sqrt{2}c_{2333} & 2c_{2323} & 2c_{2313} & 2c_{2312} \\ \sqrt{2}c_{1311} & \sqrt{2}c_{1322} & \sqrt{2}c_{1333} & 2c_{1323} & 2c_{1313} & 2c_{1312} \\ \sqrt{2}c_{1211} & \sqrt{2}c_{1222} & \sqrt{2}c_{1233} & 2c_{1223} & 2c_{1213} & 2c_{1212} \end{pmatrix}. \tag{B.15}$$

Appendix C. Notation

Abbreviations

3D	three-dimensional
BCPM	bone cell population model
BMU	basic multicellular unit
OB_a	active osteoblasts
OB_p	committed osteoblast precursor cells
OB_u	uncommitted osteoblast progenitors
OC_a	active osteoclasts
OC_p	committed osteoclast precursor cells
ODE	ordinary differential equation
OPG	osteoprotegerin
PMO	postmenopausal osteoporosis
PTH	parathyroid hormone
RANK	receptor activator of nuclear factor kappa β
RANKL	ligand of RANK
RVE	representative volume element
SED	strain energy density
TGF-β	transforming growth factor-β

Latin symbols

$a_{\mathcal{P}_{OB_p}}$	preosteoblastic proliferation fraction
$\mathbb{A}_r^{est}$	estimate of the strain concentration tensor of phase r
$\mathbb{A}_{bm}^{est}$	estimate of the strain concentration tensor of the extravascular bone matrix
$\mathcal{A}_{OB_a}$	apoptosis rate of active osteoblasts
$\mathcal{A}_{OC_a}$	maximum apoptosis rate of active osteoclasts
C_{OB_a}	molar concentration of active osteoblasts
C_{OB_p}	molar concentration of osteoblast precursor cells
C_{OB_u}	molar concentration of uncommitted osteoblast progenitor cells
C_{OC_a}	molar concentration of active osteoclasts
C_{OC_p}	molar concentration of osteoclast precursor cells
C_{OPG}	molar concentration of OPG
C_{OPG}^{max}	maximum molar concentration of OPG
C_{PTH}	molar concentration of PTH
C_{RANK}	molar concentration of RANK
C_{RANKL}	molar concentration of RANKL
C_{RANKL}^{max}	maximum molar concentration of RANKL
$C_{[RANKL-RANK]}$	molar concentration of the RANK-RANKL compound
$C_{TGF-\beta}$	molar concentration of TGF-β
$\mathbb{c}_{bm}$	microscopic stiffness tensor of extravascular bone matrix
$\mathbb{c}_{vas}$	microscopic stiffness tensor of vascular pore space
$\mathbb{C}_{cort}^{hom}$	homogenized macroscopic stiffness tensor of cortical bone
d_{RVE}	characteristic length of the heterogeneities within the RVE
$\tilde{D}_{OPG}$	constant degradation rate of OPG
$\tilde{D}_{PTH}$	constant degradation rate of PTH
$\tilde{D}_{RANKL}$	constant degradation rate of RANKL
$\tilde{D}_{TGF-\beta}$	constant degradation rate of TGF-β
$\mathcal{D}_{OB_u}$	maximum differentiation rate of uncommitted osteoblast progenitor cells
$\mathcal{D}_{OB_p}$	maximum differentiation rate of osteoblast precursor cells

$\mathcal{D}_{OC_p}$	maximum differentiation rate of osteoclast precursor cells
f_{bm}	volume fraction of the extravascular bone matrix
f_{vas}	volume fraction of the vascular pore space
$\mathbf{e}_1, \mathbf{e}_2, \mathbf{e}_3$	unit vectors
$E_{cort,ii}$	Young's moduli of cortical bone in i-direction, $i = 1, 2, 3$
$\mathbf{E}_{cort}$	macroscopic strain tensor of cortical bone
$\mathbf{E}_{cort}^{hyd}$	macroscopic hydrostatic strain tensor
$\mathbf{E}_{cort}^{shear,ij}$	macroscopic pure shear strain tensors, $ij = 12, 13, 23$
$\mathbb{I}$	fourth-order unit tensor
$\mathbb{J}$	volumetric part of $\mathbb{I}$
k_{form}	bone formation rate
k_{H_2O}	bulk modulus of water
k_{res}	bone resorption rate
$K_{d,[RANKL-RANK]}$	equilibrium dissociation binding constant for binding of RANKL to RANK
$K_{act,OB}^{PTH}$	RANKL production-relevant equilibrium dissociation constant related to binding of PTH to its receptors expressed on osteoblasts
$K_{rep,OB}^{PTH}$	OPG production-relevant equilibrium dissociation constant related to binding of PTH to its receptors expressed on osteoblasts
$K_{a,[RANKL-RANK]}$	equilibrium association binding constant for binding of RANKL to RANK
$K_{a,[RANKL-OPG]}$	equilibrium association binding constant for binding of RANKL to OPG
$K_i^{TGF-\beta}$	equilibrium dissociation constant related to TGF-β-binding to its receptors, $i = [act,OB_u]$, $[rep,OB_p]$, $[act,OC_a]$
$\mathbb{K}$	deviatoric part of $\mathbb{I}$
N_{RANKL}^{OB}	maximum number of RANKL receptors on osteoblasts
$P_{OPG,d}$	OPG dosage term
$P_{PTH,d}$	PTH dosage term
$P_{RANKL,\varepsilon_{bm}}$	"external" RANKL-dose induced by mechanical loading
p_{OB}^{OPG}	proportionality constant quantifying the OPG production of osteoblasts
$\mathbb{P}_r^{bm}$	Hill tensor of phase r embedded in a matrix with stiffness $\mathbb{c}_{bm}$
$\mathcal{P}_{OB_p}$	maximum proliferation rate of osteoblast precursor cells
ℓ_{RVE}	characteristic length of an RVE
$\mathcal{L}$	characteristic length of the geometry of a structure built up by a material defined on the RVE
$\mathcal{P}$	characteristic length of the loading of a structure built up by a material defined on the RVE
$S_{TGF-\beta}$	sink/source term of TGF-β
t	time variable
V_i	volume of phase i within an RVE
V_{total}	total volume of an RVE

Greek symbols

α	constant quantifying the content of TGF-β in the bone matrix
β_{OPG}	intrinsic OPG production rate
β_{PTH}	intrinsic PTH production rate
β_{RANKL}	intrinsic RANKL production rate

δ_{ij}	Kronecker delta
ε_{bm}	microscopic strain tensor of the extravascular bone matrix
κ	RANKL production inhibition parameter
λ	anabolic strength parameter
μ_{H_2O}	shear modulus of water
$\pi_{act,OB}^{PTH}$	activator function of effective carrying capacity of RANKL following the action of PTH
$\pi_{rep,OB}^{PTH}$	repressor function of OPG production following the action of PTH
π_{act,OC_p}^{RANKL}	activator function of osteoclast differentiation following the action of RANKL
$\pi_{act,OB_u}^{TGF\text{-}\beta}$	activator function of osteoblast differentiation following the action of TGF-β
$\pi_{act,OC_a}^{TGF\text{-}\beta}$	activator function of osteoclast differentiation following the action of TGF-β
$\pi_{rep,OB_p}^{TGF\text{-}\beta}$	repressor function of osteoblast differentiation following the action of TGF-β
Π_{act,OB_p}^{mech}	activator function of osteoblast proliferation following the mechanical loading
$\breve{\Pi}_{act,OB_p}^{mech}$	minimum value of Π_{act,OB_p}^{mech}
Σ_{cort}	macroscopic stress tensor of cortical bone
Σ_{cort}^{disuse}	macroscopic stress tensor of cortical bone under disuse conditions
Σ_{cort}^{hyd}	macroscopic stress tensor of cortical bone representing hydrostatic loading
Σ_{cort}^{normal}	macroscopic stress tensor of cortical bone under normal conditions
$\Sigma_{cort}^{shear,ij}$	macroscopic stress tensor of cortical bone representing pure shear loading, $ij = 12, 13, 23$
Σ_{cort}^{uni}	macroscopic stress tensor of cortical bone representing uniaxial loading
Ψ_{bm}	microscopic SED of extravascular bone matrix
$\breve{\Psi}_{bm}$	microscopic SED of extravascular bone matrix relating to $\breve{\Pi}_{act,OB_p}^{mech}$ and $P_{RANKL,\varepsilon_{bm}} = 0$
Ψ_{cort}	macroscopic SED of cortical bone

Mathematical symbols and operators

$\otimes$	dyadic product
:	second-order tensor contraction
$d(\cdot)/dt$	derivative of quantity $(\cdot)$ with respect to time variable t
$\ll, \gg$	symbols for "much smaller than" and "much greater than", respectively
$[\cdot]^T$	transpose of matrix $[\cdot]$

References

[1] J. Aubin, Bone stem cells, J. Cell. Biochem. 72 (Suppl. 30–31) (1998) 73–82.

[2] R. Martin, D. Burr, N. Sharkey, Skeletal Tissue Mechanics, Springer-Verlag, 1998.

[3] K. Janssens, P. ten Dijke, S. Janssens, W. Van Hul, Transforming growth factor-β1 to the bone, Endocr. Rev. 26 (6) (2005) 743–774.

[4] H. Wright, H. McCarthy, J. Middleton, M. Marshall, RANK, RANKL and osteoprotegerin in biology and disease, Curr. Rev. Musculoskelet. Med. 2 (1) (2009) 56–64.

[5] H. Frost, Dynamics of bone remodeling, in: H. Frost (Ed.), Bone Biodynamics, Little, Brown, Boston, Churchill, 1964, pp. 315–333.

[6] A. Robling, A. Castillo, C. Turner, Biomechanical and molecular regulation of bone remodeling, Annu. Rev. Biomed. Engrg. 8 (2006) 455–498.

[7] L. Bonewald, M. Johnson, Osteocytes, mechanosensing and Wnt signaling, Bone 42 (2008) 606–615.

[8] A. Santos, A. Bakker, J. Klein-Nulend, The role of osteocytes in bone mechanotransduction, Osteoporos. Int. 20 (6) (2009) 1027–1031.

[9] C. Jacobs, S. Temiyasathit, A. Castillo, Osteocyte mechanobiology and pericellular mechanics, Annu. Rev. Biomed. Engrg. 12 (2010) 369–400.

[10] L. Bonewald, The amazing osteocyte, J. Bone Miner. Res. 26 (2) (2011) 229–238.

[11] P. Pivonka, S. Komarova, Mathematical modeling in bone biology: from intracellular signaling to tissue mechanics, Bone 47 (2) (2010) 181–189.

[12] D. Webster, R. Müller, In silico models of bone remodeling from macro to nano – from organ to cell, Wiley Interdiscip. Rev. Syst. Biol. Med. 3 (2) (2011) 241–251.

[13] L. Mishnaevsky Jr., S. Schmauder, Continuum mesomechanical finite element modeling in materials development: a state-of-the-art review, Appl. Mech. Rev. 54 (1) (2001) 49–66.

[14] M. Buehler, Nanomechanics of collagen fibrils under varying cross-link densities: atomistic and continuum studies, J. Mech. Behav. Biomed. Mater. 1 (1) (2008) 59–67.

[15] Z. Yosibash, N. Trabelsi, C. Hellmich, Subject-specific p-FE analysis of the proximal femur utilizing micromechanics-based material properties, Int. J. Multiscale Comput. Engrg. 6 (5) (2008) 483–498.

[16] A. Natali, E. Carniel, P. Pavan, Investigation of bone inelastic response in interaction phenomena with dental implants, Dent. Mater. 24 (4) (2008) 561–569.

[17] R. Bhowmik, K. Katti, D. Katti, Mechanisms of load-deformation behavior of molecular collagen in hydroxyapatite–tropocollagen molecular system: steered molecular dynamics study, J. Eng. Mech. (ASCE) 135 (5) (2009) 413–421.

[18] W. Ching, P. Rulis, A. Misra, Ab initio elastic properties and tensile strength of crystalline hydroxyapatite, Acta Biomater. 5 (8) (2009) 3067–3075.

[19] C. Hellmich, F.-J. Ulm, Micromechanical model for ultra-structural stiffness of mineralized tissues, J. Engrg. Mech. (ASCE) 128 (8) (2002) 898–908.

[20] C. Hellmich, F.-J. Ulm, Drained and undrained poroelastic properties of healthy and pathological bone: a poro-micromechanical investigation, Transp. Porous Media 58 (2005) 243–268.

[21] A. Fritsch, C. Hellmich, 'Universal' microstructural patterns in cortical and trabecular, extracellular and extravascular bone materials: micromechanics-based prediction of anisotropic elasticity, J. Theor. Biol. 244 (4) (2007) 597–620.

[22] A. Fritsch, C. Hellmich, L. Dormieux, Ductile sliding between mineral crystals followed by rupture of collagen crosslinks: experimentally supported micromechanical explanation of bone strength, J. Theor. Biol. 260 (2) (2009) 230–252.

[23] C. Hellmich, F.-J. Ulm, Average hydroxyapatite concentration is uniform in the extracollagenous ultrastructure of mineralized tissues: evidence at the 110 µm scale, Biomech. Model. Mechanobiol. 2 (1) (2003) 21–36.

[24] V. Lemaire, F. Tobin, L. Greller, C. Cho, L. Suva, Modeling of the interactions between osteoblast and osteoclast activities in bone remodeling, J. Theor. Biol. 229 (3) (2004) 293–309.

[25] P. Pivonka, J. Zimak, D. Smith, B. Gardiner, C. Dunstan, N. Sims, T. Martin, G. Mundy, Model structure and control of bone remodeling: a theoretical study, Bone 43 (2) (2008) 249–263.

[26] P. Pivonka, J. Zimak, D. Smith, B. Gardiner, C. Dunstan, N. Sims, T. Martin, G. Mundy, Theoretical investigation of the role of the RANK–RANKL–OPG system in bone remodeling, J. Theor. Biol. 262 (2) (2010) 306–316.

[27] H. Frost, A determinant of bone architecture. The minimum effective strain, Clin. Orthopaed. Relat. Res. 175 (1983) 286–292.

[28] H. Frost, Perspectives: a proposed general model of the mechanostat (suggestions from a new skeletal-biologic paradigm), Anat. Rec. 244 (2) (1996) 139–147.

[29] C. Turner, Towards mathematical description of bone biology: the principle of cellular accommodation, Calcif. Tissue Int. 65 (6) (1999) 466–471.

[30] C. Hellmich, C. Kober, B. Erdmann, Micromechanics-based conversion of CT data into anisotropic elasticity tensors, applied to FE simulations of a mandible, Ann. Biomed. Engrg. 36 (1) (2008) 108–122.

[31] A. Erlebacher, E. Filvaroff, J.-Q. Ye, R. Derynck, Osteoblastic responses to TGF-β during bone remodeling, Mol. Biol. Cell 9 (7) (1998) 1903–1918.

[32] I. Owan, D. Burr, C. Turner, J. Qiu, Y. Tu, J. Onyia, R. Duncan, Mechanotransduction in bone: osteoblasts are more responsive to fluid forces than mechanical strain, Am. J. Physiol. – Cell Physiol. 273 (3) (1997) C810–C815.

[33] F. Weyts, B. Bosmans, R. Niesing, J. Van Leeuwen, H. Weinans, Mechanical control of human osteoblast apoptosis and proliferation in relation to differentiation, Calcif. Tissue Int. 72 (4) (2003) 505–512.

[34] A. Robling, P. Niziolek, L. Baldridge, K. Condon, M. Allen, I. Alam, S. Mantila, J. Gluhak-Heinrich, T. Bellido, S. Harris, C. Turner, Mechanical stimulation of bone in vivo reduces osteocyte expression of SOST/sclerostin, J. Biol. Chem. 283 (9) (2008) 5866–5875.

[35] R. Van Bezooijen, B. Roelen, A. Visser, L. Van Der Wee-Pals, E. De Welt, M. Karperien, H. Hamersma, S. Papapoulos, P. Ten Dijke, C. Löwik, Sclerostin is an osteocyte-expressed negative regulator of bone formation, but not a classical BMP antagonist, J. Exp. Med. 199 (6) (2004) 805–814.

[36] D. Winkler, M. Sutherland, J. Geoghegan, C. Yu, T. Hayes, J. Skonier, D. Shpektor, M. Jonas, B. Kovacevich, K. Staehling-Hampton, M. Appleby, M. Brunkow, J. Latham, Osteocyte control of bone formation via sclerostin, a novel BMP antagonist, EMBO J. 22 (23) (2003) 6267–6276.

[37] D. Fyhrie, D. Carter, A unifying principle relating stress to trabecular bone morphology, J. Orthopaed. Res. 4 (3) (1986) 304–317.

[38] R. Huiskes, H. Weinans, H. Grootenboer, M. Dalstra, B. Fudala, T. Slooff, Adaptive bone-remodeling theory applied to prosthetic-design analysis, J. Biomech. 20 (11–12) (1987) 1135–1150.

[39] G. Martinez, J. García-Aznar, M. Doblaré, M. Cerrolaza, External bone remodeling through boundary elements and damage mechanics, Math. Comput. Simul. 73 (1–4) (2006) 183–199.

[40] E. Ozcivici, Y. Luu, B. Adler, Y.-X. Qin, J. Rubin, S. Judex, C. Rubin, Mechanical signals as anabolic agents in bone, Nat. Rev. Rheumatol. 6 (1) (2010) 50–59.

[41] D. Jones, H. Nolte, J.-G. Scholübbers, E. Turner, D. Veltel, Biochemical signal transduction of mechanical strain in osteoblast-like cells, Biomaterials 12 (2) (1991) 101–110.

[42] D. Kaspar, W. Seidl, C. Neidlinger-Wilke, A. Beck, L. Claes, A. Ignatius, Proliferation of human-derived osteoblast-like cells depends on the cycle number and frequency of uniaxial strain, J. Biomech. 35 (7) (2002) 873–880.

[43] J. Sanz-Herrera, J. García-Aznar, M. Doblaré, Micro-macro numerical modelling of bone regeneration in tissue engineering, Comput. Methods Appl. Mech. Engrg. 197 (33–40) (2008) 3092–3107.

[44] K. Fuller, J. Lean, K. Bayley, M. Wani, T. Chambers, A role for TGF-β1 in osteoclast differentiation and survival, J. Cell Sci. 113 (13) (2000) 2445–2453.

[45] C. Liu, Y. Zhao, W.-Y. Cheung, R. Gandhi, L. Wang, L. You, Effects of cyclic hydraulic pressure on osteocytes, Bone 46 (5) (2010) 1449–1456.

[46] D. Nicolella, D. Moravits, A. Gale, L. Bonewald, J. Lankford, Osteocyte lacunae tissue strain in cortical bone, J. Biomech. 39 (9) (2006) 1735–1743.

[47] A. Rath Bonivtch, L. Bonewald, D. Nicolella, Tissue strain amplification at the osteocyte lacuna: a microstructural finite element analysis, J. Biomech. 40 (10) (2007) 2199–2206.

[48] Y. Han, S. Cowin, M. Schaffler, S. Weinbaum, Mechanotransduction and strain amplification in osteocyte cell processes, Proc. Nat. Acad. Sci. USA 101 (47) (2004) 16689–16694.

[49] A. Pitsillides, S. Rawlinson, R. Suswillo, S. Bourrin, G. Zaman, L. Lanyon, Mechanical strain-induced NO production by bone cells: a possible role in adaptive bone (re)modeling?, FASEB J 9 (15) (1995) 1614–1622.

[50] M. Mullender, A. El Haj, Y. Yang, M. van Duin, E. Burger, J. Klein-Nulend, Mechanotransduction of bone cells in vitro: mechanobiology of bone tissue, Med. Biol. Engrg. Comput. 42 (1) (2004) 14–21.

[51] X. Fan, E. Roy, L. Zhu, T. Murphy, C. Ackert-Bicknell, C. Hart, C. Rosen, M. Nanes, J. Rubin, Nitric oxide regulates receptor activator of nuclear factor-κB ligand and osteoprotegerin expression in bone marrow stromal cells, Endocrinology 145 (2) (2004) 751–759.

[52] F.-S. Wang, C.-J. Wang, Y.-J. Chen, Y.-T. Huang, H.-C. Huang, P.-R. Chang, Y.-C. Sun, K. Yang, Nitric oxide donor increases osteoprotegerin production and osteoclastogenesis inhibitory activity in bone marrow stromal cells from ovariectomized rats, Endocrinology 145 (5) (2004) 2148–2156.

[53] J. Xiong, M. Onal, R. Jilka, R. Weinstein, S. Manolagas, C. O'Brien, Matrix-embedded cells control osteoclast formation, Nat. Med. 17 (10) (2011) 1235–1241.

[54] K. Henriksen, M. Karsdal, J.-M. Delaissé, M. Engsig, RANKL and vascular endothelial growth factor (VEGF) induce osteoclast chemotaxis through an ERK1/2-dependent mechanism, J. Biol. Chem. 278 (49) (2003) 48745–48753.

[55] R. Hill, Elastic properties of reinforced solids: some theoretical principles, J. Mech. Phys. Solids 11 (5) (1963) 357–372.

[56] R. Hill, Continuum micro-mechanics of elastoplastic polycrystals, J. Mech. Phys. Solids 13 (2) (1965) 89–101.

[57] Zaoui, A. Structural Morphology and Constitutive Behavior of Microheterogeneous Materials, Springer-Verlag, Wien, New York, 1997, pp. 291–347 (Chapter 6) In [102].

[58] A. Zaoui, Continuum micromechanics: survey, J. Engrg. Mech. (ASCE) 128 (8) (2002) 808–816.

[59] C. Hellmich, F.-J. Ulm, L. Dormieux, Can the diverse elastic properties of trabecular and cortical bone be attributed to only a few tissue-independent phase properties and their interactions? – arguments from a multiscale approach, Biomech. Model. Mechanobiol. 2 (4) (2004) 219–238.

[60] C. Hellmich, Microelasticity of Bone, Springer-Verlag, Wien, New York, 2005. Chapter 8, pp. 281–331 In [101].

[61] S. Lees, J. Ahern, M. Leonard, Parameters influencing the sonic velocity in compact calcified tissues in various species, J. Acoust. Soc. Amer. 74 (1) (1983) 28–33.

[62] S. Lees, N. Tao, S. Lindsay, Studies of compact hard tissues and collagen by means of brillouin light scattering, Connect. Tissue Res. 24 (3–4) (1990) 187–205.

[63] C. Turner, J. Rho, Y. Takano, T. Tsui, G. Pharr, The elastic properties of trabecular and cortical bone tissues are similar: results from two microscopic measurement techniques, J. Biomech. 32 (4) (1999) 437–441.

[64] J. Wergedal, D. Baylink, Electron microprobe measurements of bone mineralization rate in vivo, Am. J. Physiol. 226 (2) (1974) 345–352.

[65] M. Grynpas, Age and disease-related changes in the mineral of bone, Calcified Tissue Int. 53 (S1) (1993) 57–64.

[66] B. Busa, L. Miller, C. Rubin, Y.-X. Qin, S. Judex, Rapid establishment of chemical and mechanical properties during lamellar bone formation, Calcif. Tissue Int. 77 (6) (2005) 386–394.

[67] P. Minaire, P. Meunier, C. Edouard, J. Bernard, P. Courpron, J. Bourret, Quantitative histological data on disuse osteoporosis: comparison with biological data, Calcif. Tissue Int. 17 (1) (1974) 57–73.

[68] L. Vico, P. Collet, A. Guignandon, M.-H. Lafage-Proust, T. Thomas, M. Rehailia, C. Alexandre, Effects of long-term microgravity exposure on cancellous and

[69] H. Bone, M. Bolognese, C. Yuen, D. Kendler, H. Wang, Y. Liu, J. Martin, Effects of denosumab on bone mineral density and bone turnover in postmenopausal women, J. Clin. Endocrinol. Metab. 93 (6) (2008) 2149–2157.

[70] J. Eshelby, The determination of the elastic field of an ellipsoidal inclusion, and related problems, Proc. R. Soc. Lond. Ser. A 241 (1957) 376–396.

[71] N. Laws, The determination of stress and strain concentrations at an ellipsoidal inclusion in an anisotropic material, J. Elast. 7 (1) (1977) 91–97.

[72] T. Mori, K. Tanaka, Average stress in matrix and average elastic energy of materials with misfitting inclusions, Acta Metall. 21 (5) (1973) 571–574.

[73] Y. Benveniste, A new approach to the application of Mori–Tanaka's theory in composite materials, Mech. Mater. 6 (1987) 147–157.

[74] A. Fritsch, L. Dormieux, C. Hellmich, Porous polycrystals built up by uniformly and axisymmetrically oriented needles: homogenization of elastic properties, C. R. Méc. 334 (3) (2006) 151–157.

[75] R. Ashman, S. Cowin, W. Van Buskirk, J. Rice, A continuous wave technique for the measurement of the elastic properties of cortical bone, J. Biomech. 17 (5) (1984) 349–361.

[76] P. Buenzli, P. Pivonka, B. Gardiner, D. Smith, Modelling the anabolic response of bone using a cell population model, J. Theor. Biol. 307 (1) (2012) 42–52.

[77] N. Bonnet, S. Ferrari, Exercise and the skeleton: how it works and what it really does, IBMS BoneKey 7 (7) (2010) 235–248.

[78] L. Vico, C. Alexandre, Microgravity and bone adaption at the tissue level, J. Bone Miner. Res. 7 (S2) (1992) 445–447.

[79] D. Carter, Mechanical loading histories and cortical bone remodeling, Calcif. Tissue Int. 36 (Suppl. 1) (1984) S19–S24.

[80] G. Beaupré, T. Orr, D. Carter, An approach for time-dependent bone modeling and remodeling – theoretical development, J. Ortho. Res. 8 (5) (1990) 651–661.

[81] J. García-Aznar, T. Rueberg, M. Doblaré, A bone remodelling model coupling microdamage growth and repair by 3D BMU-activity, Biomech. Model. Mechanobiol. 4 (2–3) (2005) 147–167.

[82] L. McNamara, P. Prendergast, Bone remodelling algorithms incorporating both strain and microdamage stimuli, J. Biomech. 40 (6) (2007) 1381–1391.

[83] V. Deudé, L. Dormieux, D. Kondo, S. Maghous, Micromechanical approach to nonlinear poroelasticity: application to cracked rocks, J. Eng. Mech. (ASCE) 128 (8) (2002) 848–855.

[84] B. Pichler, C. Hellmich, H. Mang, A combined fracture-micromechanics model for tensile strain-softening in brittle materials, based on propagation of interacting microcracks, Int. J. Numer. Anal. Methods Geomech. 31 (2) (2007) 111–132.

[85] D. Carter, Mechanical loading history and skeletal biology, J. Biomech. 20 (11–12) (1987) 1095–1109.

[86] R. Whalen, D. Carter, C. Steele, Influence of physical activity on the regulation of bone density, J. Biomech. 21 (10) (1988) 825–837.

[87] B. Clarke, Normal bone anatomy and physiology, Clin. J. Am. Soc. Nephrol. 3 (3) (2008) S131–S139.

[88] J. Buckwalter, M. Glimcher, R. Cooper, R. Recker, Bone biology. Part I: Structure, blood supply, cells, matrix, and mineralization, J. Bone Joint Surg. Ser. A 77 (8) (1995) 1256–1275.

[89] J. Deuerling, W. Yue, A. Espinoza Orías, R. Roeder, Specimen-specific multi-scale model for the anisotropic elastic constants of human cortical bone, J. Biomech. 42 (13) (2009) 2061–2067.

[90] X. Dong, X. Guo, Prediction of cortical bone elastic constants by a two-level micromechanical model using a generalized self-consistent method, J. Biomech. Eng. 128 (3) (2006) 309–316.

[91] M. Granke, Q. Grimal, A. Saïed, P. Nauleau, F. Peyrin, P. Laugier, Change in porosity is the major determinant of the variation of cortical bone elasticity at the millimeter scale in aged women, Bone 49 (5) (2011) 1020–1026.

[92] Q. Grimal, G. Rus, W. Parnell, P. Laugier, A two-parameter model of the effective elastic tensor for cortical bone, J. Biomech. 44 (8) (2011) 1621–1625.

[93] E. Hamed, Y. Lee, I. Jasiuk, Multiscale modeling of elastic properties of cortical bone, Acta Mech. 213 (1–2) (2010) 131–154.

[94] J. Katz, Anisotropy of Young's modulus of bone, Nature 283 (5742) (1980) 106–107.

[95] J. Martinez-Reina, J. Domínguez, J. García-Aznar, Effect of porosity and mineral content on the elastic constants of cortical bone: a multiscale approach, Biomech. Model. Mechanobiol. 10 (3) (2011) 309–322.

[96] J. Crolet, B. Aoubiza, A. Meunier, Compact bone: numerical simulation of mechanical characteristics, J. Biomech. 26 (6) (1993) 677–687.

[97] B. Aoubiza, J. Crolet, A. Meunier, On the mechanical characterization of compact bone structure using homogenization theory, J. Biomech. 29 (6) (1996) 1539–1547.

[98] U. Alon, An Introduction to Systems Biology: Design Principles of Biological Circuits, Chapman & Hall, 2007.

[99] S. Cowin, M. Mehrabadi, The structure of the linear anisotropic elastic symmetries, J. Mech. Phys. Solids 40 (7) (1992) 1459–1471.

[100] P. Helnwein, Some remarks on the compressed matrix representation of symmetric second-order and fourth-order tensor, Comput. Methods Appl. Mech. Engrg. 190 (22–23) (2001) 2753–2770.

[101] P. Suquet, Continuum Micromechanics, CISM Courses and Lectures, 377, Springer-Verlag, Wien, New York, 1997.

[102] L. Dormieux, Applied Micromechanics of Porous Media, CISM Courses and Lectures, 480, Springer-Verlag, Wien, New York, 2005.